

Peripheral positioning of lysosomes supports melanoma aggressiveness

Received: 10 September 2024

Accepted: 25 March 2025

Published online: 09 April 2025

 Check for updates

Katerina Jerabkova-Roda   1,2,3,4,5,6, Marina Peralta  1,2,3,4,5,14, Kuang-Jing Huang  1,2,3,4,5, Antoine Mousson  3,7, Clara Bourgeat Maudru  1,2,3,4,5, Louis Bochler  1,2,3,4,5, Ignacio Busnelli  1,2,3,4,5, Rabia Karali 3,7, Hélène Justiniano 3,7, Lucian-Mihai Lisii 3,7, Philippe Carl 3,7, Vincent Mittelheisser 1,2,3,4,5, Nandini Asokan 1,2,3,4,5, Annabel Larnicol 1,2,3,4,5, Olivier Lefebvre 1,2,3,4,5, Hugo Lachuer 6,8,15, Angélique Pichot 2,3,4,9, Tristan Stemmelen 2,3,4,9, Anne Molitor 2,3,4,9,10, Léa Scheid 11, Quentin Frenger 2,3,4, Frédéric Gros 2,3,4, Aurélie Hirschler 12, François Delalande 12, Emilie Sick 3,7, Raphaël Carapito 2,3,4,9,10, Christine Carapito 12, Dan Lipsker 11, Kristine Schauer 6,8,16 & Philippe Rondé 3,7,16 & Vincent Hyenne 1,2,3,4,5,13,16 & Jacky G. Goetz 1,2,3,4,5,16

Emerging evidence suggests that the function and position of organelles are pivotal for tumor cell dissemination. Among them, lysosomes stand out as they integrate metabolic sensing with gene regulation and secretion of proteases. Yet, how their function is linked to their position and how this controls metastasis remains elusive. Here, we analyze lysosome subcellular distribution in patient-derived melanoma cells and patient biopsies and show that lysosome spreading scales with melanoma aggressiveness. Peripheral lysosomes promote matrix degradation and cell invasion which is directly linked to the lysosomal and cell transcriptional programs. Using chemo-genetical control of lysosome positioning, we demonstrate that perinuclear clustering impairs lysosome secretion, matrix degradation and invasion. Impairing lysosome spreading significantly reduces invasive outgrowth in two *in vivo* models, mouse and zebrafish. Our study provides a direct demonstration that lysosome positioning controls cell invasion, illustrating the importance of organelle adaptation in carcinogenesis and suggesting its potential utility for diagnosis of metastatic melanoma.

Metastases are responsible for the majority of cancer-related deaths¹. Melanoma shows strong negative correlation between cancer stage and 5-year patient survival, making it an ideal model to study phenotypic changes leading to cancer cell invasion, adaptation and survival. Melanoma progression consists of multiple sequential events and its early detection is key for patient survival. First, melanocytes are

transformed and grow in the epidermis during radial growth phase (RGP), forming a lesion with low potential to develop metastasis. Changes in their transcription program lead to expression of matrix-degrading enzymes and to invasion through the dermis during vertical growth phase (VGP) followed by cancer dissemination through vascular and lymphatic routes, progressing into metastatic stages². To

A full list of affiliations appears at the end of the paper.  e-mail: katerina.jerabkova@inserm.fr; kristine.schauer@gustaveroussy.fr; philippe.ronde@unistra.fr; hyenne@unistra.fr; jacky.goetz@inserm.fr

colonize secondary organs during metastasis, melanoma cells sense their microenvironment and react by locally degrading the extracellular matrix (ECM), consisting of structural and specialized proteins (collagen, fibronectin, laminin), which can be remodeled by various proteases, allowing cell dissemination to adjacent tissues³. This suggests that melanoma metastasis requires specific invasion programs for an efficient, targeted delivery and exocytosis of ECM-degrading enzymes. Such programs could involve the MITF/TFE transcription factors, which are often amplified in melanoma⁴ and control various catabolic functions of lysosomes, including their exocytosis⁵.

While the implication of lysosome secretion in cell migration has been recently unveiled, how it is orchestrated in invasive cells and whether it might regulate the progression of the disease remains unclear. Distinct reports indicated that lysosomes constitute emerging regulators of invasion by allowing cells to sense their microenvironment and trigger adapted responses, notably through the exocytic release of their content⁶. For instance, lysosomal exocytosis drives the formation of invasive protrusions resulting in basement membrane breaching in *C. elegans*⁷. In addition, secretion of lysosomal cathepsin B promotes cancer cell invasion and metastasis⁸. Besides, lysosome secretion contributes to the repair of plasma membrane damages occurring during cell migration and results in better cell survival under mechanical stress⁹.

Importantly, lysosomal activity is regulated by their subcellular location^{10,11}. Peripheral lysosomes are prone to exocytosis and drive growth factor signaling¹², while perinuclear lysosomes have a decreased pH and higher proteolytic activity¹⁰. Lysosome distribution is in turn directly impacted by endosomal phosphoinositide levels¹³ or the cellular microenvironment¹⁴. Lysosomes are transported to the plasma membrane via kinesins (anterograde transport) in response to growth factors and nutrients' presence, conversely, during starvation and in alkaline environment, lysosomes are transported to the perinuclear region (retrograde transport) in a dynein-dependent manner⁶.

While the molecular mechanisms driving lysosomal positioning have been broadly studied¹⁵⁻¹⁷, little is known about the *in vivo* functional implications of these changes and whether they can control invasion programs of melanoma cells and their metastatic progression. To answer this question, several studies have described the consequences of manipulating genes involved in lysosome transport on tumor cell invasion¹⁸⁻²². However, knockdown strategies often impact secondary functions of targeted genes, raising doubts on the precise contribution of lysosome positioning defects in tumor progression. To circumvent these limitations and to fill such gap, we use a unique chemo-genetic tool to control lysosome positioning and to fully demonstrate that lysosomal secretion, regulated via its positioning, controls melanoma invasiveness and impacts its metastatic potential. We reveal a phenotypic switch in the positioning of lysosomes in aggressive melanoma that is supported by distinct transcriptional programs and controls migration and invasion. When impairing the peripheral positioning of lysosomes using a chemo-genetic approach applicable to *in vitro* and *in vivo* models, we reduced the invasion potential of melanoma cells. Importantly, we provide primary evidence in human biopsies that lysosomal positioning strictly correlates with the metastatic progression of the disease. Our study not only illustrates the importance of organelle adaptation in carcinogenesis by providing direct evidences that lysosomal positioning controls secretory pathways of malignant transformation, it also reveals a unique lysosomal phenotype, which could potentially be used for the diagnosis of metastatic melanoma.

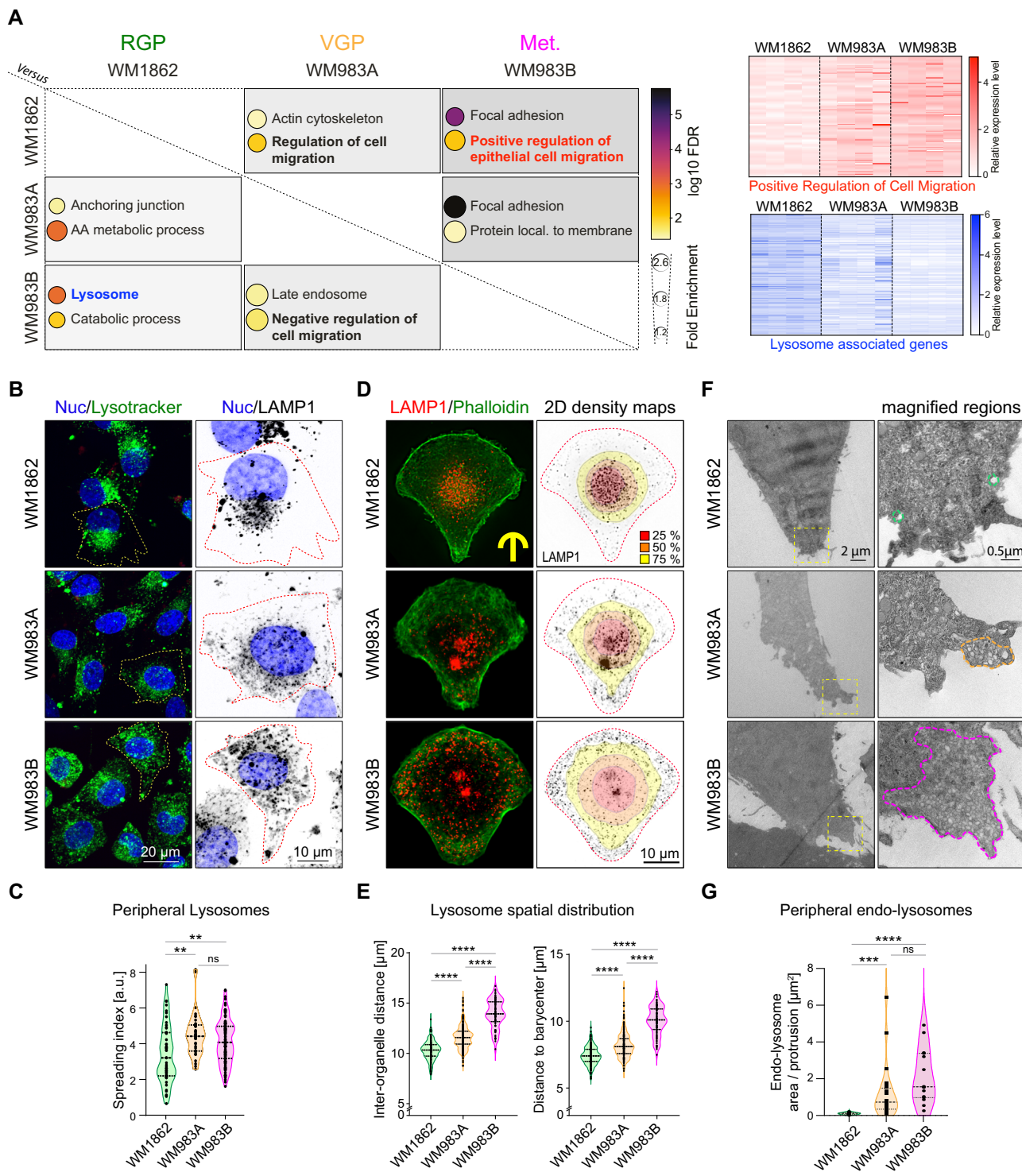
Results and discussion

Melanoma invasiveness scales with lysosome spreading

Cells progressing through the metastatic cascade display tremendous phenotypic plasticity in the benefit of increased invasion and ECM degradation potential. In order to investigate invasion-promoting

properties, we first characterized a collection of patient-derived melanoma cells from different stages (RGP: WM1552c, WM1862, VGP: WM115, WM983A and metastatic: WM983B, A375 cells). With a collagen invasion assay (Fig. S1A), we identified three groups of patient-derived cell lines with low, medium and high invasion potential (Fig. S1B), which correlated with their cancer progression state (RGP, VGP and metastatic). Using gelatin degradation assay (Fig. S1C), we further showed that cells with high invasion index displayed significantly increased gelatin degradation area and frequency (Fig. S1D, E), in accordance with our earlier observations²³. While gelatin degradation areas were located at invadopodia, specifically identified by the invadopodia markers actin and cortactin (Fig. S1C, F), they transiently colocalized with LAMP1, a marker of late endosomes and lysosomes (referred to as lysosomes hereafter) (Fig. S1F-H), suggesting that gelatin degradation might involve dynamic shuttling and targeting of lysosomes. These acidic organelles contain metalloproteases (MMPs) and cathepsins that could be released by exocytosis when lysosome transiently co-localize with invadopodia to favor ECM degradation²⁴. Indeed, the concerted expression of matrix-degrading enzymes has been previously associated with the transition of melanoma cells from RGP to VGP². To identify the underlying mechanisms, we assessed transcriptional profiles of the three, representative patient-derived cell lines of increasing invasion index (WM1862, WM983A, WM983B) using RNAseq and Gene Ontology analysis. This showed an overrepresentation of actin cytoskeleton and cell migration pathways associated with a concomitant reduction of transcripts linked to the lysosomal pathway and metabolism in WM983B cells (Fig. 1A and Table S1, S2). We thus hypothesized that increased invasion occurs through a phenotypic switch from a catabolic, lysosomal signature characteristic of RGP cells (WM1862) to a migratory signature found in metastatic cells (WM983B). As lysosome function is linked to its position¹⁰, we investigated their sub-cellular localization in these cell lines by live imaging of freely growing cells and observed that metastatic cells have increased localization of lysosomes to cell periphery as quantified by their 2D radial distribution (Fig. 1B, C, Fig. S2A, B). We analyzed lysosome positioning in cells plated on micropatterns, which allows for high-throughput study of cells with reproducible shapes (Fig. 1D left) and facilitates the comparison and quantitative analysis of lysosome distribution in 2D (Fig. 1D right) and in full cell volume (Fig. S2C). While RGP cells had mostly perinuclear lysosomes, metastatic cells showed significant dispersion of LAMP1-compartments towards the cell periphery (Fig. 1D) characterized by a significant increase in the mean inter-organelle distance and the mean distance to their barycenter (Fig. 1E). Moreover, LAMP1-compartments were smaller and more abundant, but globally similarly acidic and degradative in metastatic cells (Fig. S2D, E), revealing that the observed transcriptional changes in melanoma cells correlate with changes in LAMP1 distribution. Unbiased analysis of organelles using electron microscopy of the three cell lines revealed strong accumulation of late endosomes/lysosomes in peripheral and protrusive regions of metastatic cells (Fig. 1F, G).

Our results identify and characterize an important cellular phenotype of spread lysosomes associated with aggressive malignancy in melanoma. Since peripheral lysosome positioning has been reported earlier in other cancer types (breast cancer²² and bladder cancer¹³), we next investigated potential molecular mechanisms underlying this phenotype. Transcriptomics data analysis demonstrates that genes known to promote perinuclear localization of lysosomes, such as *RILP*⁷ or *RNF167*²⁵, show decreased expression, and conversely, genes linked to anterograde transport, such as *KIF1B* and *KIF5B*²⁶, are overexpressed in metastatic cells (Fig. S3A). Besides, other lysosomal genes previously associated with cancer progression such as *LAMP1*^{21,27}, lysosomal Ca²⁺ channel *MCOLN1*⁵ and several metalloproteases³ (*MMP2*, *MMP15*, *MMP17*) are also upregulated in metastatic cells (Fig. S3A). To probe the molecular mechanism promoting lysosome spreading in



melanoma, we focused on the two kinesins, *KIF1B* and *KIF5B*, whose expression levels gradually increase with the aggressiveness of patient-derived cell lines (Fig. S3B). When any of the two kinesins was downregulated using siRNA (Fig. S3C, D), lysosomes relocalized from the periphery to the perinuclear region (Fig. S3E, F). In addition, we analyzed sequencing data of primary and/or metastatic melanomas from 331 patients, available at the TCGA database²⁸. Interestingly, both *KIF1B* and *KIF5B*, show an increased expression in samples of metastatic melanomas when compared to primary tumors (Fig. S3G), suggesting that they could, in part, be responsible for a correlation between lysosomal positioning and melanoma progression.

In patients with metastatic melanoma, lysosomes are relocated to the cell periphery

Following our observations in patient-derived cell lines, we tested whether changes in lysosome positioning can also be observed in biopsies from melanoma patients and whether specific patterns correlate with the progression stage. For that purpose, we analyzed lysosome subcellular distribution in samples from human biopsies of healthy skin, benign naevi, primary melanoma and melanoma skin metastases (Fig. 2A). Notably, while Sox10-positive melanocytes of healthy and benign tissues displayed strong lysosome perinuclear clustering, cells of melanoma cutaneous metastases showed prominent peripheral positioning of lysosomes (Fig. 2B, C). In the primary

Fig. 1 | Melanoma invasiveness correlates with lysosome spreading.

A Transcriptomics comparison of melanoma cells reveals increased expression of genes regulating cell migration and decreased expression of lysosome-associated genes in metastatic cells, quadruplicate. Differentially expressed genes ($p\text{Adj} < 0.01$) were analyzed using gene ontology (GO). Left: Selected GO terms are listed, showing their fold enrichment and \log_{10} FDR in paired comparisons, Right: Heatmaps for two main pathways identified, white = low expression, blue/red = high expression. **B, C** Lysosome positioning in non-constrained cells, live cell imaging. **B** Representative images: NucBlue (nucleus), green lysotracker (lysosomes). WM1862 $n = 51$, WM983A $n = 40$, WM983B $n = 108$ cells, in triplicate. **C** Spreading index, CellProfiler (Mean \pm SD) = 3.390 ± 1.597 , 4.477 ± 1.180 , 4.111 ± 1.225 , respectively. p values (from top) = 0.0069 , 0.0011 , 0.6009 , one dot = 1 cell. **D, E** Lysosome positioning in melanoma cells on micropatterns. **D** Left: Immunofluorescence (max z-projection), Right: overlay of LAMP1 signal and 2D density maps showing LAMP1 distribution (R software), displaying the smallest area occupied by 25% (red), 50% (orange) and 75% (yellow) of all compartments. **E** Left: Inter-organelle distance

(IOD) = average of distances between all lysosomes. IOD (Mean \pm SD) = 10.30 ± 0.94 , 11.56 ± 1.15 , 13.99 ± 1.40 , respectively. One dot = 1 cell, $p < 0.0001$ in all conditions. Right: Distance to barycenter (DB) = distance from each lysosome to the geometric center (lysosomes). DB (Mean \pm SD) = 7.40 ± 0.69 , 8.21 ± 0.93 , 10.03 ± 1.07 , respectively. One dot = 1 cell, $p < 0.0001$ in all conditions. WM1862, $n = 182$ cells, WM983A, $n = 231$ cells, WM983B, $n = 82$ cells, in triplicate. **F, G** Electron microscopy reveals that the presence of endolysosomal compartments in protrusions scales with melanoma aggressiveness. **F** Representative images, endolysosome-rich regions in protrusions are circled in dashed lines, color-coded per melanoma stage. **G** Area occupied by endo-lysosomes in protrusions: WM1862 $n = 14$, WM983A $n = 24$, WM983B $n = 15$, Area \pm SD = 0.1075 ± 0.05614 , 1.219 ± 1.474 , 2.106 ± 1.457 , respectively. One dot = 1 field of view, p values (from top): < 0.0001 , 0.1672 , 0.0001 . * $p < 0.05$; ** $p < 0.01$; *** $p < 0.001$; **** $p < 0.0001$. All statistics are done using Kruskal-Wallis with Dunn's multiple comparison post-hoc test. Source data are provided as a Source Data file.

melanoma, lysosome spreading was variable but rather low when compared to metastatic melanoma, suggesting that peripheral lysosomes are only appearing in cells that are bound to be metastatic, and could potentially serve as a prognostic marker. In addition, while the naevi samples displayed heterogeneous positioning of lysosomes, the proportion of cells with peripheral lysosomes increased with the depth away from the epidermis (Fig. 2D, E), suggesting that more complex programs might be at play to stimulate the changes in lysosome positioning and to promote tumorigenesis. Whether this is also true for primary melanoma remains to be investigated as the lesions were too small to perform spatial analysis. Taken together, these results show that lysosome spreading correlates with melanoma stage, in particular, metastatic melanoma cells redistribute their lysosomes towards cell periphery, as seen in collection of tumor biopsies from a cohort of patients. Our results connect lysosome spreading to melanoma metastasis and support the importance of this phenotype for future clinical applications as for example, improving the classification criteria for malignant and non-malignant lesions and thus allowing for early detection of lesions with metastatic potential and timely intervention.

Forcing lysosome perinuclear clustering in metastatic melanoma cells

To study the consequences of lysosome repositioning for metastatic evolution of melanoma, we engineered melanoma cells employing a chemo-genetic strategy based on the fast and strong heterodimerization of the FKBP and FRB domains by Rapalog²⁹. We chose WM983A and WM983B cell lines, derived from the primary tumor and metastatic site of the same patient, respectively. We stably expressed FKBP domain fused to LAMP1 and the FRB domain fused to dynein adaptor BicD2 (Fig. 3A). Rapalog treatment induced binding of BicD2 and recruitment of Dynein to LAMP1, forcing lysosome movement towards the minus end of microtubules, and thus perinuclear clustering of the LAMP1 compartment around the microtubule organizing center (Fig. 3B, S4F). Clustering was fast, dose-dependent (Fig. S4A, B) and persistent in time (Fig. S4C, D, E), as previously described²⁹, allowing precise control of lysosomal positioning in vitro and in vivo. Engineered control cells expressing only single domain FKBP (FKBP only) did not show lysosome clustering upon Rapalog treatment (Fig. S4A, C, D). Correlative light and electron microscopy (CLEM) of control- or Rapalog-treated WM983B-LAMP1-mCherry cells showed colocalization between LAMP1-mCherry and vesicular compartments, which clustered as expected in the perinuclear region upon Rapalog treatment (Fig. 3C). Notably, Rapalog does not impair the colocalization between LAMP1-mCherry and the BODIPY-Pepstatin A (Fig. S4G), which is delivered to lysosomes via endocytic pathway³⁰ and binds to the active site of cathepsin D in acidic conditions, suggesting that clustering by Rapalog did not disrupt cargo delivery and lysosomal

catabolic activity in melanoma cells. Accordingly, global lysosome mass and acidity are not affected by Rapalog-induced lysosome clustering (Fig. S4H). Of note, Rapalog is a chemically modified analog of Rapamycin unable to bind lysosome-related mTOR and to thus perturb mTORC1 signaling³¹. Accordingly, we could not detect any changes in mTORC1 signaling in our model under normal conditions of culture (Fig. S4I–J). As such, this tool brings great advantage over genetic studies targeting the known regulators of lysosome positioning as it allows to reposition specifically the LAMP1 positive organelles without impacting secondary functions of selected genes, caused by protein depletion. Proteins controlling lysosome positioning often have other functions: KIF1B and KIF5B for instance are known to regulate the localization of other organelles, endosomes and mitochondria^{32,33} while RILP controls lysosomal pH³⁴ and RNF167 regulates ubiquitination²⁵. By contrast, Rapalog can be used to study the direct link between lysosome position and cancer invasiveness.

Peripheral lysosomes promote secretion and matrix degradation

Lysosome exocytosis of different proteases and subsequent extracellular matrix degradation promotes invasion to adjacent tissues^{7,35}. We thus first investigated how altering positioning of the LAMP1 compartment impacts the cell secretome. We analyzed the concentrated cell supernatant of WM983B cells in the presence and absence of Rapalog treatment by mass spectrometry (Fig. 3D, Table S3) and by human protease array (Fig. S5A, Table S4). Together, these results show an overall decrease in the total protease content secreted by the cells when lysosomes are clustered close to the nucleus (Fig. S5A, Table S3, S4). We identified a significant decrease of several lysosome-associated proteins upon lysosome perinuclear clustering, including cathepsins and various metalloproteases from the ADAM, Kallikrein and MMP families (Fig. 3D, Table S3, S4). These enzymes contribute to ECM degradation³⁶, tumor growth and invasion³⁷ and they have been linked to metastatic progression, for instance in the case of cathepsin S or B in gastric and colorectal cancers, respectively^{8,38}. To confirm that Rapalog-induced perinuclear clustering inhibits lysosome exocytosis, we imaged VAMP7-pHluorin, a v-SNARE involved in the fusion of lysosome with plasma membrane^{39,40} using TIRF microscopy (Fig. 3E, F). Quantification reveals that cells with perinuclear clustering showed significantly reduced numbers of VAMP7 secretory events (Fig. 3G, H, Fig. S5B), with no impact on the duration of the secretion process (Fig. 3I). These experiments demonstrate that perinuclear clustering of lysosomes impairs lysosome exocytosis by metastatic melanoma cells. These results are in line with a previous observation of peripheral lysosomes promoting their fusion with plasma membrane and thus exocytosis in a model of lysosomal storage disease⁵. Next, we investigated whether perinuclear lysosome clustering would impair the ECM degradation machinery

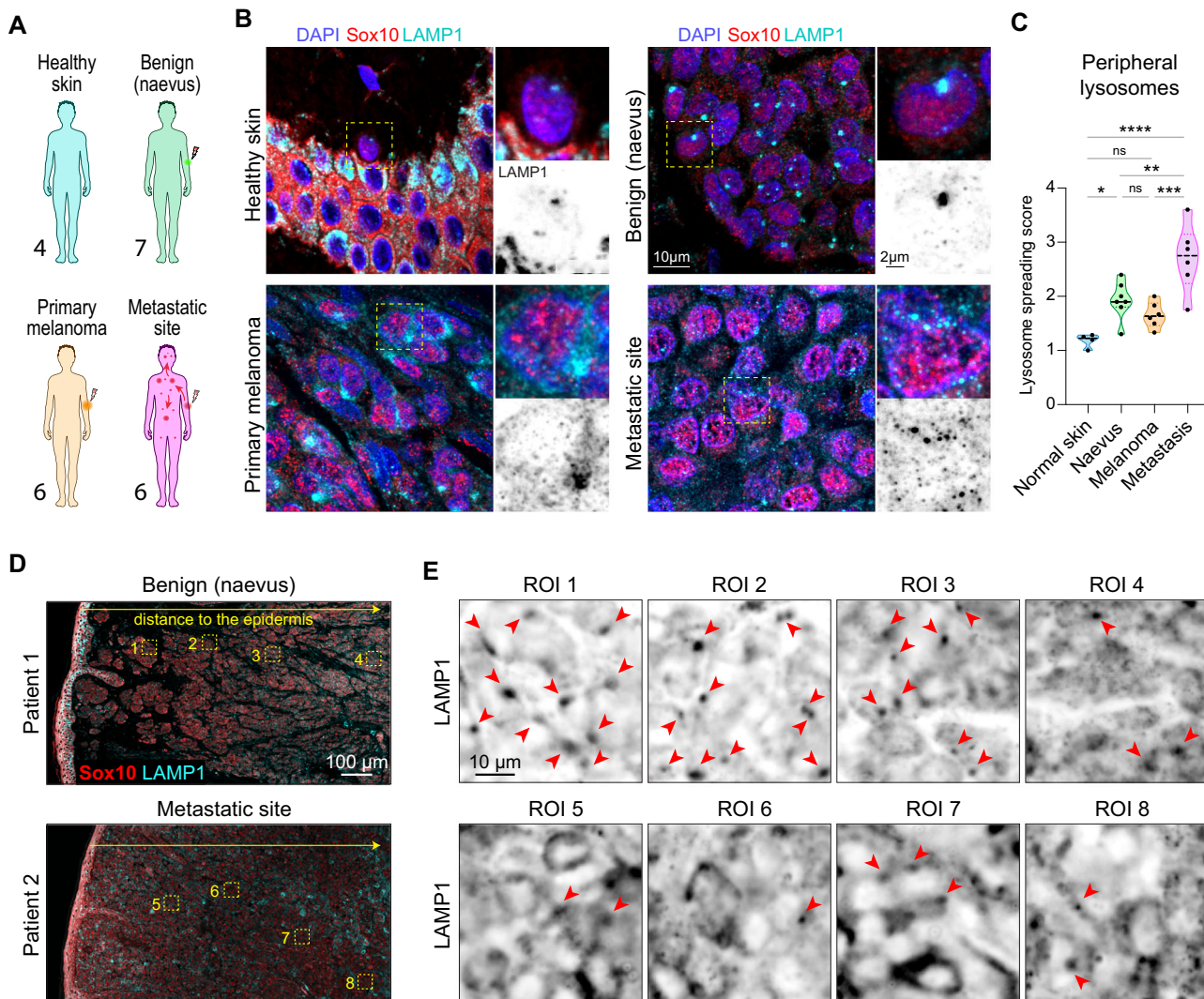


Fig. 2 | Lysosomes spread as melanoma progresses towards metastasis in human biopsies. **A** Samples of patient biopsies were obtained from healthy skin donors ($n = 4$) and from patients with benign tissue (nevus, $n = 7$), primary melanoma ($n = 6$) and metastatic melanoma (skin metastasis, $n = 6$). Silhouettes (Servier medical art CC:BY 4.0 license) are color-coded according to melanoma stage. **B** Representative images of patient biopsies sections: samples were labeled for SOX10 (red), LAMP1 (cyan) and nuclei (blue) by immunofluorescence, full tissue section was imaged by slide scanner. **C** Quantification of lysosome spreading. Ten random regions were analyzed in a blinded setup for lysosome positioning. Lysosome spreading score, range 1–4: (Mean \pm SD) = 1.184 ± 0.1276 , 1.929 ± 0.3450 , 1.656 ± 0.2373 , 2.793 ± 0.6094 , respectively. One dot represents 1 patient, p values

(from top, left) = <0.0001 , 0.1544 , 0.0087 , 0.0218 , 0.2298 , 0.0010 , ordinary one-way ANOVA with Holm-Sidak's test, * $p < 0.05$; ** $p < 0.01$; *** $p < 0.001$; **** $p < 0.0001$. **D, E** Lysosome spreading shows a spatial heterogeneity within the tumor mass. **D** Representative images of biopsies from patient 1 (benign tissue, nevus) and patient 2 (metastatic melanoma). Low magnification image mapping the tissue section, stained for LAMP1 (cyan), SOX10 (red) by immunohistochemistry, 2 patients per group. **E** Zoomed regions from panel (D), showing the progressive change in lysosome spreading with increasing distance to the epidermis, single channel: LAMP1 antibody staining. Red arrows point to clustered lysosomes. Source data are provided as a Source Data file.

(Fig. 4). Gelatin degradation area was reduced in both the primary tumor (WM983A) and the metastatic cells (WM983B) upon perinuclear lysosome clustering (Fig. 4A, B, Fig. 4C, D). While degradation frequency in WM983A (VGP) cells remained unaltered (Fig. 4E), the metastatic WM983B cells showed a significant decrease upon lysosome peri-nuclear clustering (Fig. 4F). We then tested the impact of forced peri-nuclear clustering of lysosomes on invasion of melanoma cells (Fig. 4G). Untreated cells (FKBP-FRB) and Rapalog-treated control cells (FKBP only) have peripheral lysosomes, which were perinuclear in Rapalog-treated cells expressing both FKBP-FRB domains (Fig. 4G bottom). Rapalog treatment alone had no effect on the invasion index, but Rapalog-induced perinuclear lysosome clustering significantly decreased the invasion potential of the metastatic melanoma cells (Fig. 4H). Similarly, preventing lysosome spreading by depleting either KIF1B or KIF5B resulted in decreased melanoma invasion (Fig. 4I).

These results further confirmed that peripheral lysosome positioning promotes lysosome exocytosis which contributes to ECM degradation and cell invasion. Forcing perinuclear lysosome localization rescues these phenotypes, suggesting that lysosome position and subsequent secretion promotes ECM remodeling, as often seen in aggressive cancers⁴¹. More globally, cancer cell secretion is likely to further shape pro-metastatic features of the tumor microenvironment, and to favor the emergence of, for example, cancer associated fibroblasts, whose ECM remodeling expertise is pivotal during tumor progression^{42,43}. Of note, we have observed transient localization of lysosomes to invadopodia, in line with earlier observation that targeted secretion of CD63-positive multi-vesicular bodies promotes invadopodia formation⁴⁴. Yet, while LAMP1 is highly enriched in protrusive regions of melanoma cells, its co-localization with invadopodia markers was only partial and transient, suggesting that lysosomal exocytosis likely

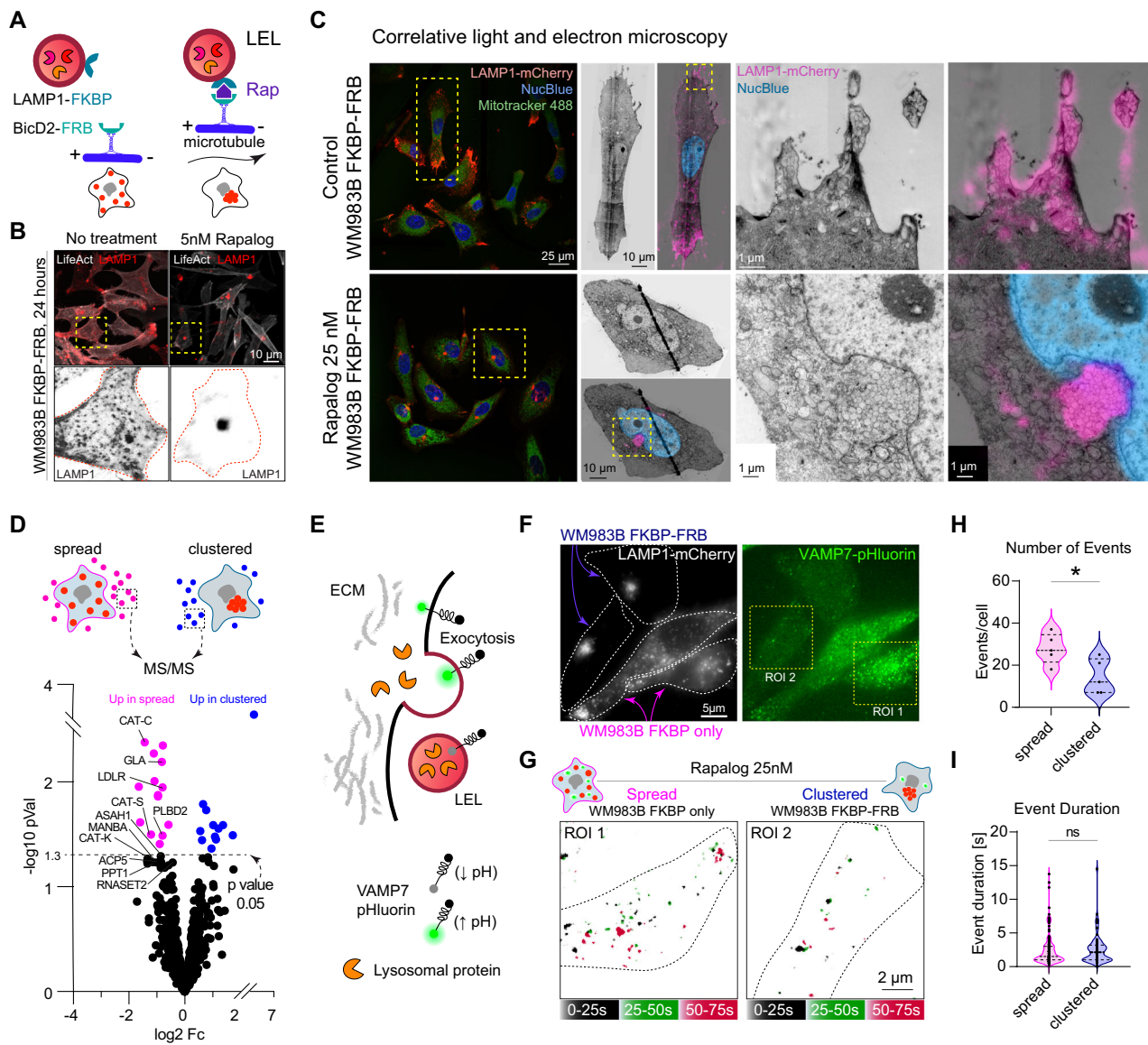


Fig. 3 | Lysosome perinuclear clustering inhibits lysosome exocytosis.

A, B Rapalog-mediated perinuclear clustering of lysosomes. **A** Lysosomes in WM983B cells stably expressing LAMP1-mCherry-FKBP and BicD2-FRB can be clustered using Rapalog compound (Rap) which induces FKBP-FRB rapid heterodimerization. **B** Representative images of lysosome perinuclear clustering 24 h after 5 nM Rapalog treatment. **C** Correlative light and electron microscopy of clustered perinuclear LAMP1 positive compartments. Representative immunofluorescent images and a high magnification overlay of fluorescent and electron microscopy images (LAMP1 in red/magenta, nucleus in blue) are shown for each condition, in duplicate. **D** Melanoma secretome is altered by lysosome perinuclear clustering. Differential quantitative mass spectrometry analysis of proteins secreted to the cell medium by WM983B (FKBP-FRB) cells in the absence or presence of 5 nM Rapalog. Proteins known to be lysosome-associated are labeled with their name. Magenta = proteins upregulated in cells with spread lysosomes, blue = proteins upregulated in cells with clustered lysosomes ($p < 0.05$). Differential analysis was done using Limma moderated t test with adaptive Benjamini-Hochberg procedure to adjust the p values. **E–I** Rapalog-induced perinuclear clustering

inhibits lysosome exocytosis. **E** Lysosome secretion was assessed by TIRF microscopy using VAMP7-pHluorin probe, which is quenched in lysosome acidic environment and brightly fluorescent once exposed to the alkaline pH of the extracellular space. **F** Representative images of co-cultured WM983B-LAMP1-mCherry cells expressing either single heterodimerizing domain (FKBP only, magenta) or both the domains (FKBP-FRB, blue) treated with 25 nM Rapalog, TIRF microscopy. **G** TIRF movie was divided into three time-segments (black: 0–25 s, green: 25–50 s, dark red: 50–75 s) and displayed as maximum projection showing the number of events per each time-segment. Two representative examples: ROI 1 = spread lysosomes, ROI 2 = clustered lysosomes. **H, I** Quantification of the TIRF movie. **H** Number of lysosome secretion events in 1 min, one dot = 1 cell. **I** Event duration, one dot = 1 event, $n = 5$ cells. Events per cell (Mean \pm SD): spread = 27.80 ± 7.19 , clustered = 14.40 ± 8.23 , p value = 0.0397. Event duration (Mean \pm SD): spread = 2.46 ± 2.36 , clustered = 2.56 ± 2.20 s, p value = 0.3518. Mann–Whitney test, two-tailed with Dunn's multiple comparison post hoc test. Source data are provided as a Source Data file.

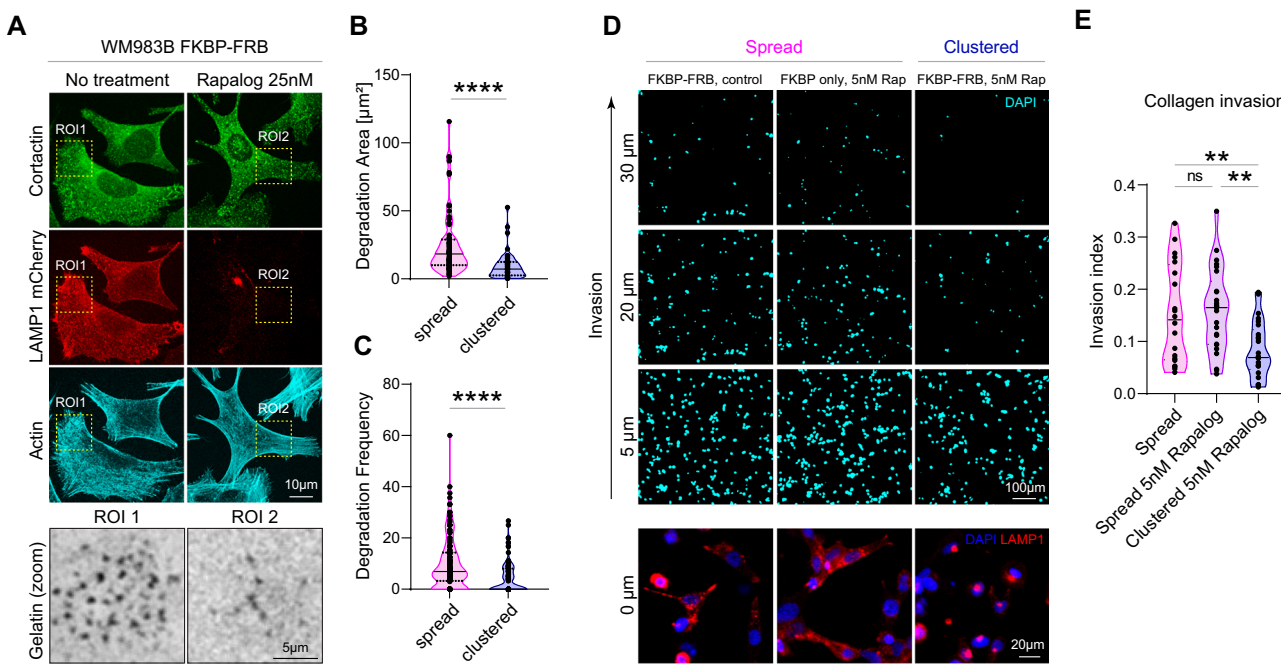


Fig. 4 | Lysosome clustering impairs matrix degradation and cell invasion. A–C Peripherally positioned lysosomes promote gelatin degradation. **A** Representative images of WM983B cells (LAMP1-mCherry-FKBP-FRB) with spread lysosomes (medium) and clustered lysosomes (5 nM Rapalog), cultured on FITC-gelatin (gray), stained for cortactin (green), LAMP1 (red) and actin (cyan), in triplicate. **B** Degradation Area (Mean \pm SD) = 24.75 \pm 23.29 n = 73 cells, 4.91 \pm 9.94 n = 50 cells, respectively, p value: <0.0001 , Mann–Whitney test, two-tailed. One dot represents 1 cell. **C** Degradation frequency (Mean \pm SD) = 10.14 \pm 10.45 n = 138 cells, 4.43 \pm 6.04 n = 102 cells, respectively, p value: <0.0001 , Mann–Whitney test, two-tailed. **D, E** Lysosome perinuclear clustering decreases collagen invasion, live cell imaging.

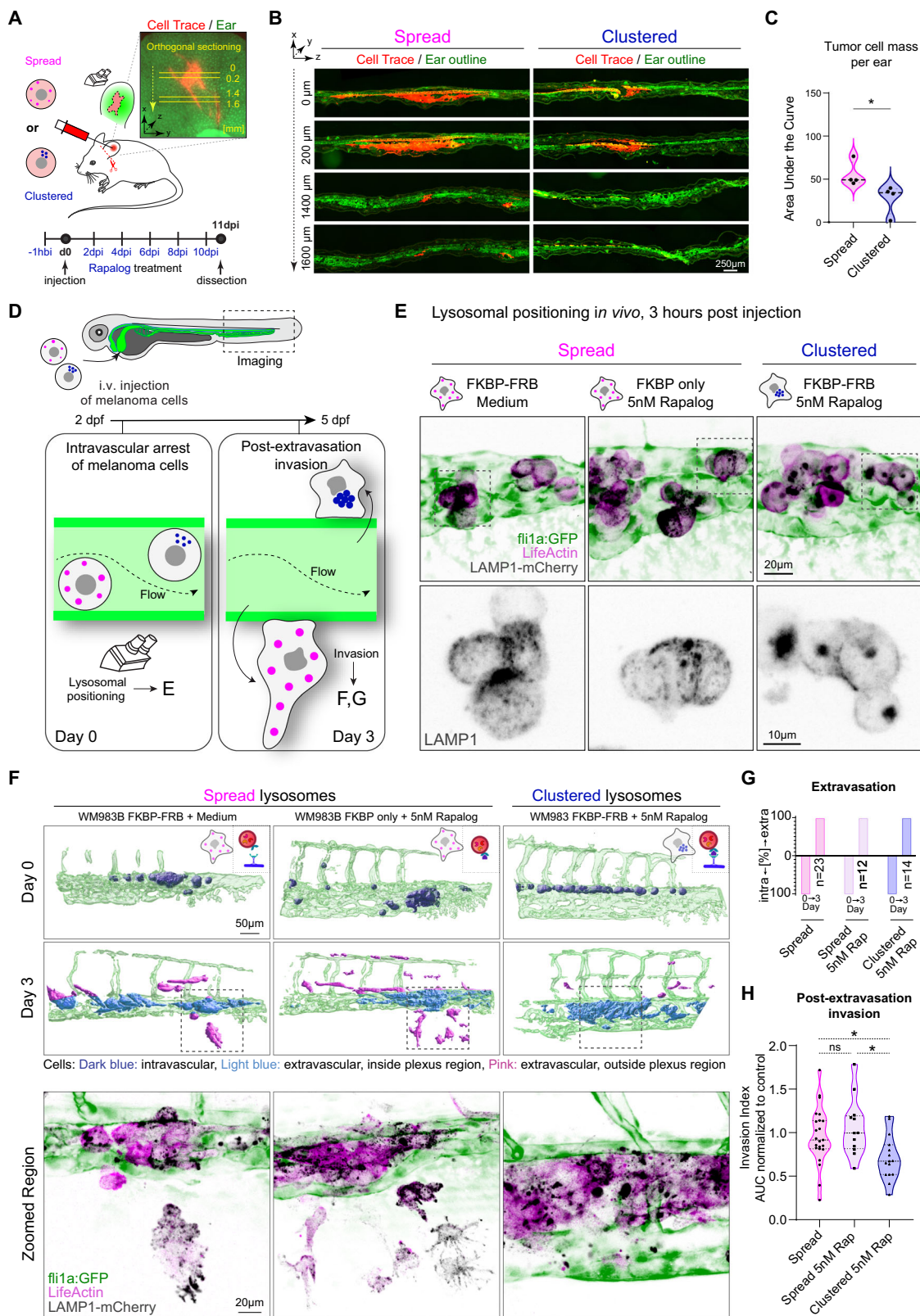
D Bottom: Representative images of WM983B cells with spread lysosomes (FKBP-FRB control and FKBP only with Rapalog 5 nM) and clustered lysosomes (FKBP-FRB with 5 nM Rapalog), nucleus (blue), lysosomes (red). Top: Representative images of cell invasion after 24 h, nucleus (cyan). **E** Quantification of the invasion index: FKBP-FRB (spread) n = 20, FKBP only (spread) n = 25, FKBP-FRB (clustered) n = 25, (Mean \pm SD) = 0.1526 \pm 0.094, 0.1592 \pm 0.079, 0.0836 \pm 0.053, respectively, in triplicate, p value (from top, left) = 0.0067, 0.7728, 0.0023, ordinary one-way ANOVA, Holm–Sidak multiple comparison test. One dot represents 1 field of view. * p < 0.05; ** p < 0.01; *** p < 0.001; **** p < 0.0001. Source data are provided as a Source Data file.

occurs outside of active invadopodia as well. It has been reported that microtubule-transported post-Golgi carriers are secreted near focal adhesions, which capture and stabilize microtubules⁴⁵. Lysosomal exocytosis visualized by VAMP7-pHluorin can occur at focal adhesions⁴⁰ that have been associated with invasive matrix degradation⁴⁶. Alternatively, CD63+ late endosomes/lysosomes are re-localized to the cell periphery and protrusive structures, where they could, for example, promote the secretion of pro-tumorigenic extracellular vesicles⁴⁴. Whether distinct types of late endosomes act in concert to favor ECM degradation, or whether it involves hybrid late endo-lysosome compartments remains to be determined.

Forcing lysosomal clustering impairs invasion potential of melanoma cells

Building on the stability of Rapalog-mediated lysosomal clustering in patient-derived cells and the demonstration that it impairs ECM degradation and cell invasion in vitro, we sought to monitor if lysosome position impacted melanoma dissemination in vivo. We first set up an experimental approach based on subcutaneous grafting of fluorescently-labeled (Cell Trace) melanoma cells in ears of nude mice (Fig. 5A). Tumors made of control cells (FKBP only) and cells with both FKBP-FRB domains were subjected to topic treatment with Rapalog (5 nM) every 2 days. Rapalog treatment alone had no effect on cell proliferation or cell viability in vitro (Fig. S5F, G). Upon 11 days of growth and dissemination, we serially sectioned the ears and quantified the range of invasion. Tumors (n = 4) made of melanoma cells with peripheral lysosomes displayed increased levels of dissemination (Fig. 5B, C) as quantified by the area of fluorescently-labeled cells in each section (Fig. S6A). In contrast, melanoma tumors (n = 4) with

perinuclear lysosome clustering displayed limited dissemination potential (Fig. 5B, C) demonstrating that forced perinuclear clustering of lysosomes impairs the metastatic properties of melanoma tumors in vivo. To further demonstrate that melanoma invasiveness is altered by lysosome perinuclear clustering, we switched to an alternative experimental metastasis model where invasion can be tracked in real time. To do so, we injected melanoma cells with different lysosome clustering status intravenously in two days post-fertilization zebrafish embryos⁴⁷ to probe lysosomal clustering while assessing the metastatic and invasive potential of melanoma cells over time (Fig. 5D, Fig. S6B). Lysosome clustering was stable in vivo and visible in round circulating tumor cells that had just arrested in the vasculature after injection (Fig. 5E) as well as in the growing non-invasive tumor cells three days post injection (Fig. 5F, bottom). At day 3, while all melanoma cells had efficiently extravasated (Fig. 5G), independently of their lysosomal positioning, cells with peripheral lysosomes displayed increased post-extravasation invasion potential in vivo (Fig. 5H, Fig. S6C, D). Notably, Rapalog treatment alone had no impact on the invasion index (Fig. 5H) when we compared untreated cells (FKBP-FRB) and Rapalog-treated control cells (FRB only) which both have spread lysosomes (Fig. 5E, F). On the contrary, when lysosomes were clustered in melanoma cells before injection, their ability to invade after extravasation was strongly impaired (Fig. 3F, H). Collectively, these data show that lysosome positioning is an important driver of melanoma invasiveness, both at the level of the primary tumor (Fig. 5A–C) and in metastatic dissemination (Fig. 5D–H). As seen in our study, cells with peripheral lysosomes have higher invasion potential in vitro as well as in vivo, which can be rescued by promoting the perinuclear lysosome clustering and thus reducing their malignancy, providing the first



in vivo molecular control of lysosome positioning in metastatic progression.

Organelles are dynamic, self-organized structures whose specific function is inevitably linked to their position and morphology⁴⁸, in space and time within cells^{6,49}. In this study, we provide direct demonstration that the position of lysosomes within cells tightly controls the targeted secretion of matrix-degrading enzymes which

subsequently promotes melanoma cell invasion and metastatic progression. While our work provides a direct link with melanoma metastasis, a recent study shows that relocalization of lysosomes to the cell periphery promotes the emergence of leader cells in collective epithelial cell migration⁵⁰. Re-positioning at the periphery enables localized secretion of proteolytic enzymes contained in lysosomes at focal adhesion⁴⁰, invadopodia⁵¹ or within broader protrusive regions of

Fig. 5 | Lysosome clustering impairs cancer cell invasion in vivo. **A–C** Lysosome clustering prevents tumor cell invasion in mice. Cells with spread (FKBP only, 5 nM Rap) and clustered (FKBP-FRB, 5 nM Rap) lysosomes were injected intradermally in mouse ear. **B** Representative Immunofluorescence examples of mouse ear sections. Red = tumor cells, green = ear (autofluorescence). **C** Quantification of cell mass in the ears when lysosomes are spread and clustered ($n = 3$ mice, 4 tumors per group), calculated from cell area per each section and distance in tumor: (Mean \pm SD) = 55.06 ± 14.47 , 27.55 ± 17.34 , respectively, p value 0.0286, Mann–Whitney test, two-tailed. **D–H** Perinuclear lysosome clustering prevents cell invasion in zebrafish. **D** Illustration of the invasion assay in zebrafish. *Flt1a*:GFP (green endothelium) zebrafish embryos (48 hpf) were injected intra-vascularly with WM983B cells and imaged at day 0 and day 3 post injection to assess the post-extravasation invasion potential of cancer cells with different lysosomal positioning. **E** Representative confocal images of WM983B cells (stably expressing LAMP1-mCherry= black, and LifeActin-miRFP670= magenta) with spread (FKBP-FRB control; FKBP only 5 nM

Rapalog) and clustered (FKBP-FRB, 5 nM Rapalog) lysosomes at 3 h post-injection shown as maximum z projection, in triplicate. **F** Top: IMARIS segmentation, representative examples at day 0 (3 h after cell injection) and at day 3 (72 h post injection). Bottom: Zoomed regions showing confocal images corresponding to the IMARIS segmentation at day 3. Images are shown as a maximum z projection (LAMP1-mCherry= black, LifeActin-miRFP670= magenta, vasculature= green). **G** Quantification of cell extravasation at day 0 and day 3. Negative axis= intravascular cells, positive axis= extravascular cells. **H** Post-extravasation invasion (PEI) potential (day 3) was calculated as a ratio: area of cells that migrated outside of the vasculature region to the total area of cells. FKBP-FRB (spread) $n = 23$ embryos, FKBP only (spread) $n = 12$ embryos, FKBP-FRB (clustered) $n = 15$ embryos, PEI (Mean \pm SD) = 0.9616 ± 0.3284 , 1.060 ± 0.3316 , 0.7085 ± 0.2568 , respectively, in triplicate, p values (from top, left) = 0.0317 , >0.9999 , 0.0172 , Kruskal–Wallis with Dunn's test. One dot= 1 fish, normalized to spread condition. * $p < 0.05$; ** $p < 0.01$; *** $p < 0.001$; **** $p < 0.0001$. Source data are provided as a Source Data file.

the cell. While more work is required to understand the switches that relocalize lysosomes, our study demonstrates that peripheral lysosome positioning promotes cell invasion through lysosomal secretion and ECM remodeling and thus contributes to metastatic progression. In addition, although we did not detect any change in lysosomal degradative capacities upon lysosome peri-nuclear clustering, it could potentially alter tumor progression by mediating nutrient sensing^{41,42} or chemoresistance through the secretion of therapeutics stored in lysosomes²¹. Our study exploited a chemo-genetic model of forced lysosome clustering which requires cell engineering and would therefore benefit from the complementary use of small molecules that regulate lysosome positioning, particularly for clinical applications. We previously identified PI3K inhibitors as potent lysosome clustering agents in bladder cancer¹³. Indeed, lysosome positioning, and more general organelle topology⁵², were used as a readout in a screen for alternative therapeutic drugs and targets⁵³. This opens an exciting area of research leading to a wider drug discovery approach centered on organelle positioning.

Probing of spatial distribution and morphology of lysosomes in human tumors could constitute an indicator of tumor progression, as it is the case for cell shape or additional morphometric analysis^{54,55}. We now demonstrate that lysosomal peripheral distribution can be used as a proxy for melanoma metastatic dissemination. We further show that deeply invading cells away from the epidermis tend to display increased lysosome spreading as if such repositioning increased with the invasive properties of cells. This suggests that probing lysosomal positioning could allow to refine classification criteria for malignant and non-malignant cutaneous lesions. Several other organelles, such as mitochondria, are intimately linked to cancer progression and probing simultaneously multiple organelles, as it can be done using whole-cell segmentation of high-resolution images⁵⁶, could document precisely which organelles, and their contacts, are repositioned during melanoma progression. Interestingly, deep learning-based approaches recently demonstrated the power of correlating breast cancer status with organelle topology, which out-performed morphology-based features, further highlighting the need to consider organelles positioning, and their interactome, as a cancer rheostat that could be exploited for better diagnosis⁵².

Methods

All animals were housed and handled according to the guidelines of INSERM and the ethical committee of Alsace (CREMEAS), following French and European Union animal welfare guidelines (Directive 2010/63/EU on the protection of animals used for scientific purposes. All procedures were performed in accordance with French and European Union animal welfare guidelines and supervised by local ethics committees. Zebrafish facility A6748233; APAFIS 2018092515234191). Mouse facility agreement number: #C67-482-33; APAFIS #43901-

2023062112024760 and #49848-2024061215501273-V5. All procedures performed in studies involving human participants are in accordance with the ethical standards of the institutional and/or national research committee (CE-2024-79) and with the 1964 Helsinki declaration and its later amendments or comparable ethical standards. Patient informed consent was collected and the project was approved by the Ethic committee from the Hôpitaux Universitaires de Strasbourg (CE-2024-79).

Antibodies

Anti-Cortactin (p80/85) clone 4F11 (ref. n°05-180-I) and Anti-LAMP1 (ref. n°L1418) are from Merck (Sigma-Aldrich) and anti-SOX10 (ref. 383R-10) is from Cell Marque. Alexa FluorTM 488 Phalloidin (ref. n° A12379), Alexa FluorTM 568 Phalloidin (ref. n°A12380), Alexa FluorTM 647 Phalloidin (ref. n°A22287) and Alexa Fluor-conjugated secondary antibodies, are all from Thermo Fisher Scientific. Secondary antibodies: Alexa FluorTM 405 conjugated Goat anti-Rabbit (ref. n°A-31556), Alexa FluorTM 488 conjugated Goat anti-Rabbit (ref. n°A-11034), Alexa FluorTM 555 conjugated Goat anti-Rabbit (ref. n°A21429) & Alexa FluorTM 647 conjugated Goat anti-Rabbit (ref. n°A-21244).

Cell Culture

Primary human melanoma cell lines were purchased from Rockland and cultured in MCDB153 (ref. P04-80062, Dutscher) and Leibovitz's L-15 medium (ref. n°11415064, Thermo Fisher Scientific) in a 4 to 1 ratio, supplemented with 2% fetal bovine serum, 1.68 mM CaCl₂ and 1% penicillin/streptomycin. All cell lines were purchased from Rockland: WM1552C (WM1552C-01-0001) and WM1862 (WM1862-01-0001) are non-tumorigenic (RGP) primary human melanoma cell lines without metastatic capability. WM115 (WM115-01-0001) and WM983A (WM983A-01-0001) are tumorigenic (VGP) human primary melanoma cell line. WM983B (WM983B-01-0001) is a human metastatic melanoma cell line derived from the same patient as WM983A. All cell lines are mutant for BRAF^{V600E}.

Western blot

Cell extracts were prepared in presence of phosphatase inhibitors (Ref. A32961, Thermo Fisher Scientific) when needed and denatured in Laemmli buffer and incubated at 95 °C for 10 min. 40 µg of protein extract were loaded on 4–20% polyacrylamide gels (Bio-Rad Laboratories, Inc). The following antibodies were used: Rabbit anti-KIF1B (Ref. A301-055A, Thermo Fisher Scientific), rabbit anti-KIF5B (Ref. ab167429, Abcam), mouse anti-GAPDH (Ref. MAB374, Millipore), rabbit anti-4EBP1 (Ref. 9644 T, Cell Signaling), rabbit anti-Phospho-4EBP1 (Ref. 2855, Cell Signaling), rabbit anti-p70S6K (Ref. 2708 T, Cell Signaling), rabbit anti Phospho-p70S6K (Ref. 9234, Cell Signaling) and Secondary horseradish peroxidase-conjugated antibodies: anti-Mouse (Ref. 715-035-151, Interchim) and anti-rabbit (Ref. 111-035-003, Jackson

ImmunoResearch). Acquisitions were performed using iBright 1500 (Thermo Fisher) imager. Intensities were measured using the Fiji software.

Lentivirus transduction, plasmid transfection, siRNA silencing

Transduction. pLSFFV-LAMP1-mCherry-FKBP (FK506 binding protein), pLSFFV-BicD-FRB (FKBP-rapamycin binding domain) and pLSFFV-LifeActin-miRFP lentivirus were produced in HEK293T cells using JetPRIME® transfection reagent (Polyplus). WM983B cells were infected by lentivirus in the presence of 5 µg/mL polybrene (ref. n°TR-1003, Merck/Sigma-Aldrich) followed by antibiotic selection (puromycin 1 µg/mL, blasticidin 5 µg/mL, hygromycin 200 µg/ml).

Transfection. Cenexin-GFP plasmid was transfected using JetOPTIMUS® transfection reagent (Polyplus) in a live-video dish, 46 h prior experiment.

siRNA silencing. Cells were reverse-transfected with siRNA from Dharmacon 30 nM; ON-Targetplus human KIF1B (L-009317-00), human KIF5B (L-008867-00) and Non-targeting Pool (D-001810-10) using Lipofectamin RNAiMAX (ThermoFisher Scientific, Ref. n°13778150) and analyzed after 72 h for knockdown efficiency by western blot and for lysosome positioning with Lysotracker by confocal imaging as described below.

Collagen invasion assay

Melanoma cell lines at 3×10^5 cells/ml were labeled with Hoechst 33342 and suspended in 3 mg/mL of serum free solution of neutralized Type I Bovine Collagen (PureCol® 5005-B, Advanced Biomatrix). Then, 600 µL were distributed into black 24 well plates (ref. n°058062, Dutscher) coated with bovine serum albumin or in 4-chamber glass bottom dishes (Cellvis). The plates were centrifuged at $650 \times g$ at 4 °C for 5 min and incubated at 37 °C for 2 h. Once collagen had polymerized, medium supplemented with 10% fetal bovine serum, 100 ng/mL EGF was added on top of the collagen. 24 h after, cells were observed using a Leica TSC SPE confocal microscope (x20 HCX PI Apo 0.7 NA objective, Wetzlar, Germany) and z-stacks were acquired. Four fields per sample were imaged. Nuclear localization was quantified by IMARIS (interactive microscopy image analysis software) in each field of view. The invasion index was calculated as the number of nuclei above 10 µm (Fig. S1B), 15 µm (Fig. S3H) 20 µm (Fig. 4E) divided by the total number of nuclei by field. See⁵⁷ for more information.

Matrix degradation assay and immunofluorescence

Coating. Glass coverslips were washed (20% nitric acid) for 30 min, followed by 120 min wash (deionized water), poly-L-lysine coating (50 µg/ml, prechilled), 20 min and 3x wash in PBS. Coverslips were incubated with 0.5% glutaraldehyde, 15 min and then coated with 0.2% FITC gelatin or Cy3 gelatin (G13187, Sigma Aldrich). See⁵⁸ for more details.

Degradation assay. starved melanoma cells expressing or not LAMP1-mCherry-FKBP and BicD2-FRB were plated on fluorescent gelatin and incubated at 37 °C for 6 to 24 h in medium supplemented with 10% fetal bovine serum with or without Rapalog. Cells were fixed using 4% paraformaldehyde permeabilized using triton-X-100 at 0.1% and incubated in 2% of bovine serum albumin at room temperature. Cells were then labeled for 1 h with Cortactin (1/250) antibody. After three washes with PBS, cells were incubated with secondary antibody (Alexa Fluor™ 405 conjugated Goat anti-Rabbit, 1/1000) and Alexa Fluor™ 647 Phalloidin (1/250) for 1 h, washed and mounted in ProLong™ Gold Antifade Mountant (ref. n°P10144, Thermo Fisher Scientific). Cells were imaged using Leica TSC SPE or SP8 confocal microscope (x63 HCX PI Apo 1.40 NA or x20 HCX PI Apo 0.7 NA objective, Wetzlar,

Germany). Invadopodia were identified as actin and cortactin rich punctate structure. Areas of degradation were identified as “black holes” within the fluorescent gelatin. Invadopodia and areas of degradations were quantified using ImageJ software (v1.51q). Degradation areas measurements were based on cells displaying degradation activity, and the frequency of degradation was based on randomly selected cells. Maximum filter, background subtraction and gaussian blur filters were then applied to extract the gel degradation areas by thresholding. Then, M1 Manders coefficients between LAMP1 and inverted Gelatin intensity pictures for these selections were calculated using the colocalization finder plugin.

Clustering dynamics, washout experiments & proliferation assay

Mechanism of lysosome clustering. clustering was performed by heterodimerization between LAMP1-mCherry-FKBP (lysosomes) and BicD-FRB (dynein adaptor) by the use of Rapalog (A/C Heterodimerizer ref. n°635057, from Takara Bio Inc., also known as AP21967). Cells were cultured in glass bottom dishes and imaged at different time points (24, 48 and 72 h) using Olympus Spinning Disk (60X objective, N.A. 1.2). To establish time needed for lysosome clustering, WM983A and WM983B cells expressing both heterodimerizing domains (FKBP-FRB) were treated with 5 nM or 25 nM Rapalog and followed in time. Time to appearance of lysosome cluster was counted.

Washout experiments. WM983B cells expressing either one (FKBP only) or two (FKBP-FRB) heterodimerizing domains were cultured in medium supplemented with 5 nM or 25 nM Rapalog. To assess the stability of clustering, cells were treated for 1 h with 5 nM or 25 nM Rapalog, washed 3x in PBS and cultured in normal medium for the duration of the experiment. Cells cultured in normal growth medium were used as a control.

Proliferation assay. proliferation rates of WM983B cells treated with increasing concentrations of Rapalog were analyzed using the Incucyte® Live-Cell Analysis System. Confluences were automatically calculated by the Incucyte® software based on bright field images, all values are normalized to time zero. Acquisition was performed for 96 h.

Micropatterning & Immunofluorescence

Micropatterns were prepared using photo-lithography methods as previously described^{48,59}. Briefly, cover slides were cleaned in EtOH, dried, cleaned with UV for 10 min, coated in PLL-PEG and exposed to UV 10 min through a Photomask with 36 µm crossbow micropatterns. Coverslips were coated in Fibronectin (40 µg/ml—ref. n°F1141 Merck/Sigma-Aldrich). WM1862, WM983A, WM983B cells were trypsinized, resuspended in 5 ml culture medium and seeded on micropatterned coverslips. Cells were let to spread for 4 h before fixing them in 4% PFA. For micropatterning, cells were fixed in 4% PFA, washed 3x in PBS, permeabilized in saponin 0.5% / 2% BSA in PBS for 20 min, blocked 30 min in 2% BSA, stained with Anti-LAMP1 (ref. n°L1418) primary antibody for 1 h, washed 3x in PBS, stained with Alexa Fluor™ 555 secondary Goat anti-Rabbit (1:500) and Alexa Fluor™ 488 Phalloidin (1:200) 45 min. Mounted in Fluoromount-G™ mounting medium ref. n°00-4958-02, Thermo Fisher Scientific with DAPI. High resolution, volume imaging was achieved using Olympus Spinning Disk (60X objective, N.A. 1.2) / Delta Vision—Advanced Precision (100X oil objective, U PL S APO, NA 1.4) with CoolSNAP HQ2 CCD camera (1392 × 1040 pixels). Large z-stacks were acquired for the full cell volume (0.2 µm step between layers). Image analysis and processing were performed using the Fiji (1.51q)⁶⁰, Metamorph and R software, allowing for precise calculation of lysosome volume and number.

Patient samples

Samples from tumor biopsies. Samples were provided by the Laboratoire d'Histopathologie Cutanée de la Clinique Dermatologique des Hôpitaux Universitaires de Strasbourg. Patient written informed consent was collected and the project was approved by the Ethic committee from the Hôpitaux Universitaires de Strasbourg (CE-2024-79). There was no selection based on gender, race, ethnicity or age.

TCGA data analysis. The Cancer Genome Atlas Program (TCGA). We analyzed data set from TCGA SKCM database containing 333 primary and/or metastatic melanomas from 331 patients²⁸ using UCSC Xena platform⁶¹.

Patient biopsies: immunohistochemistry, imaging, quantification

Paraffin-embedded 4µm sections were rehydrated (toluene–ethanol–PBS), followed by antigen retrieval (5 min boiling in 10 mM sodium citrate #C9999 Sigma-Aldrich), permeabilized 2 × 10 min in PBS (0.3% Triton X100), blocked 1 h (3% BSA, 20 mM MgCl₂, 0.3% Tween 20, 5% FBS) and incubated with primary antibodies (LAMP1 #L1418, SOX10 #383R-14) overnight at 4 °C, followed by 1 hr staining with secondary antibodies (1:250 dilution) and mounted in Fluoromount DAPI. Full tissue section was imaged using Slide Scanner (Olympus, 20x objective).

Quantification was done in a blinded setup, analyzing 23 samples of patient biopsies. Ten regions of interest were randomly selected per each patient sample, reaching 240 individual regions, which were randomized and then a score between 1 and 4 was given to each region based on the level of lysosome spreading (1 = 0–25% spread, 2 = 25–50% spread, 3 = 50–75% spread, 4 = 75–100% spread). Average score per patient sample was calculated and after that samples were annotated and plotted in the graph showing Healthy skin: 4 patients, Nevus: 7 patients, Primary melanoma: 6 patients, Metastatic site: 6 patients.

Live cell imaging

For live cell imaging, wild-type patient-derived cells treated with 50 nM Green Lysotracker (Molecular Probes #L7526) or WM983A and WM983B cells, stably expressing LAMP1-mCherry and LifeAct-miRFP were plated on fibronectin-coated (Sigma-Aldrich F1141, 10 µg/ml in water) 4-chamber glass bottom dishes (35 mm, #1.5, Cellvis) or on fluorescent gelatin-coated coverslips mounted in a Ludin Chamber (Life Imaging Services), respectively.

Gelatin degradation. The cells were placed at 37 °C, 5% CO₂ on an iMIC microscope equipped with a multi-LED Lumencor Spectra X. Images were acquired with an Olympus 60x TIRFM (1.45 NA) objective every 2.5 min during 4 h and a Hamamatsu Flash 4 V2+ camera (Iwata) piloted by the Live Acquisition software (Till Photonics). Expressing cells were initially located via both the mCherry and LifeAct-miRFP signals, and were subsequently followed via dual phase contrast/fluorescent signal together with the FITC-coupled gelatin substrate. 10 to 20 different fields were sequentially recorded during each experiment using a Marzhauser Motorized Stage piloted by the iMIC software. JeasyTFM software were then used for automatic selection and repositioning of the best focused images in all channels and time-points. Mean fluorescence intensity of actin, Lamp1 and the underlying substrate at each time points were calculated at invadopodia identified using gelatin degradation.

Lysosome radial distribution. The cells were placed at 37 °C, 5% CO₂ chamber on an Olympus Spinning Disk (60X objective, N.A. 1.2) and full cell volume z-stacks (0.5µm step) were acquired and then processed in ImageJ (1.53t) and CellProfiler (4.2.1)⁶². Analysis was done on Maximum intensity projections, cell outline was manually segmented

in ImageJ, nuclei were segmented based on thresholding of DAPI channel in ImageJ. Binary masks were processed in CellProfiler and radial distribution was calculated using green lysotracker signal.

TIRF microscopy. WM983B cells expressing FKBP only (spread) and WM983B cells expressing both FKBP and FRB (clustered) were mixed in a 1:1 ratio, seeded in fibronectin-coated low glass bottom µ-Dish 35 mm (ref. n°80137, Ibidi) 48 h prior to imaging, treated with 25 nM Rapalog for 1 h. Imaging was performed in culture medium using an inverted Leica DMI8 microscope (objective 100X HC PL APO 1.47 oil). Recording was done with an Evolve® 512 camera (for TIRF-HILO), at 512 × 512 pixels resolution, at an acquisition rate of 250 ms between frames, for a total duration of 90 s, with AFC (Adaptive Focus Control). Exocytosis events were identified based on VAMP7-pHluorin signal, marking lysosome exocytosis¹⁰. Secretion events were detected and counted manually.

Human protease array

Cells were seeded on collagen, cultured for 48 h in serum-free medium and conditioned medium was analyzed using a human protease array (RnDSystems, ARY021B), following the manufacturer's instructions.

Flow cytometry

Cells were seeded at a density of 1×10^5 cells per well in 96-well plates (Falcon® 353077) and labeled 30 min at 37 °C 5% CO₂ with either 50 nM Lysotracker™ Green DND-26 (Invitrogen™ L7526), 1 µM LysoSensor™ Green DND-189 (Invitrogen™ L7535) or Magic Red® Cathepsin B (1:26 dilution, IMC 937) diluted in 100 µL of culture medium. Cells were washed with PBS, resuspended in 300 µL of BSA 2% in PBS and analyzed by flow cytometry (Attune NxT, Invitrogen™). Geographic mean fluorescent intensities were determined with FlowJo V10 (LLC).

Intradermal ear injection in mouse

Six to eight-week old female immunodeficient nude mice (CrI:NU(NCr)-FoxnInu; Charles River) were used in all experiments. Mice ears were injected intradermally with 250 000 WM983B cells of different lysosome clustering status (FKBP only spread; FKBP-FRB clustered) diluted in 20 µl PBS and previously labeled with eBioscience eFluor 670 (ThermoFisher Scientific, ref. 65-0840-85) and treated with 5 nM Rapalog 1 h before injection. Subsequently, mice were treated every day with local application of Rapalog (5 nM) on the ear. At day 11, ears were harvested, imaged by fluorescence, embedded in OCT (Cellpath) and frozen at -80 °C. 7µm transversal ear sections were performed with a cryostat, mounted with Fluoromount-GTM with DAPI (ThermoFisher Scientific, ref. 00-4959-52). Maximum tumor size allowed by the local ethical committee (0.5 cm³) was not exceeded. Imaging was performed using a slide scanner (Olympus, 20X objective) and area covered by tumor cells (Cell Trace fluorescence) was measured in ImageJ and plotted over the section number (= distance in tumor) using GraphPad Prism.

Experimental metastasis assay in zebrafish

Tg(fli1ae:GFP)⁶³ embryos were maintained in Danieau 0.3X medium (17.4 mM NaCl, 0.2 mM KCl, 0.1 mM MgSO₄, 0.2 mM Ca(NO₃)₂) buffered with HEPES 0.15 mM (pH=7.6), supplemented with 200 µM of 1-phenyl-2-thiourea (PTU, ref. n°P7629, Merck/Sigma-Aldrich) to avoid pigmentation. Two days post-fertilization (2dpf) embryos were mounted in 0.8% ultrapure low melting point agarose (Invitrogen) containing 0.17 mg/ml tricaine (ethyl-3-aminobenzoate-methane-sulfonate, ref. n°E10521, Merck/Sigma-Aldrich). WM983B cells of different lysosome clustering status (spread, clustered) were injected with a Nanoject II Auto-Nanoliter Injector (Drummond Scientific Company) and microforged glass capillaries (25 to 30µm inner diameter) filled with mineral oil (ref. n°M5904, Merck/Sigma-Aldrich). 13.8nL of cell suspension from confluent T25 flasks (50 × 10⁶ cells per

ml approx.) were injected in the duct of Cuvier under a M205 FA Fluorescence stereomicroscope (Leica), as previously described⁶⁴. Embryos were injected with WM983B cells or with WM983B cells treated with 5 nM rapalog 1 h prior to injection, and then kept in Danieau with PTU. Caudal plexus was recorded at day 0 (injection day) and 3dpi using the inverted spinning-disk Olympus IXplore Spin, 30x / 1.05 NA (silicone) objective. Z-stacks of the caudal plexus were acquired for each embryo (3 μ m or 5 μ m between layers, at day 0 and 3dpi respectively) with the following settings: 488 nm laser at 2% for 100 ms / 561 nm laser at 15% for 300 ms / 640 nm laser at 15% for 300 ms. Detailed lysosome status (Fig. 5E) was imaged at 3 hpi using a 60x/1.2 NA (water) objective.

Correlative light and electron microscopy (CLEM)

WM983B cells expressing LAMP1-mCherry-FKBP and BicD2-FRB were cultured in control medium, or in medium supplemented with 25 nM Rapalog for one hour and imaged with an Olympus Spinning Disk (60X objective, N.A. 1.2). The samples were then chemically fixed right after the photonic acquisition with 0.05% malachite green, 2.5% glutaraldehyde in 0.1M sodium cacodylate buffer (NaCac), pH7.4 during 30 min in an ice bath. Subsequently the samples were post-fixed in 1% OsO₄ - 0.8% K₃[Fe(CN)₆] - 0.1M NaCac buffer pH7.4 (under a fume hood) kept in an ice bath for 50 min, and then washed 2 times with in ice-cold 0.1 M NaCac. Then the samples were incubated in 1% aqueous tannic acid solution for 25 min in an ice bath and finally washed 5 times with distilled water. Samples were then kept in 1% uranyl acetate aqueous solution overnight at 4 °C sheltered from the light. The samples were serially dehydrated with ethanol solutions (25%, 50%, 70%, 95% and 100%). Subsequently the samples were incubated in a serial resin-ethanol 100% mix (1:3; 1:1; 3:1), ending with an incubation in 100% Epon resin 3 times 1 h at room temperature. The samples were allowed to polymerize in an oven at 60 °C for 48 h. The resin blocks were trimmed by ultramicrotomy, 90 nm thin sections were collected and placed in copper/formvar slot grids. The transmission electron microscopy (TEM) data sets were acquired with a Hitachi 7500 TEM, with 80 kV beam voltage, and the 8-bit images were obtained with a Hamamatsu camera C4742-51-12NR. Correlative light and electron images were obtained/combined using Adobe Photoshop v.24.4.

Transmission electron microscopy

WM1862, WM983A, and WM983B cells were seeded on Aclar® films (EMS) and were fixed in primary fixation buffer containing 2.5% glutaraldehyde (EMS) and with 0.05% malachite green (Sigma-Aldrich) in 0.1M cacodylate buffer (EMS) for 30 min on ice. Following post-fixation were processed in 1% OsO₄ and 0.8% K₃[Fe(CN)₆] in 0.1M cacodylate buffer on ice for 50 min, and then incubated in 1% aqueous tannic acid solution for 25 min. Cells were stained with 1% uranyl acetate, and then dehydrated in sequential gradient alcohol baths and infiltrated with Epon resin. The resin polymerization is cured in an oven at 60 °C for 48 h. Ultrathin sections (90 nm) were obtained by Leica ultramicrotome, and collected serial sections on a copper grid for TEM observation. Finally, the ultra-sections were post-stained by UranyLess (EMS) for 10 min, and rinsed several times with H₂O followed by 3% Reynolds lead citrate (EMS) for 10 min. Micrographs were obtained at 80 kV in Hitachi 7500 TEM with Hamamatsu camera C4742-51-12NR digital camera. Area of protrusions containing endo-lysosomes was analyzed in imageJ (Fiji, v1.53t).

Image analysis

Organelles segmentation was performed using MetaMorph Microscopy Automation and Image Analysis Software (Molecular Devices) and the ImageJ Modular Image Analysis (MIA) plugin. Segmentation on LAMP1 images were performed to get coordinates for individual LAMP1+ objects and their number. 3D Density maps and inter-organelle distance and distance to barycenter were obtained

through the use of R software. Codes are available on GitHub⁶⁵ (https://github.com/KJerabkovaRoda/Lysosome_positioning). Cell invasion in zebrafish was performed by ImageJ (v1.53t) & Cell Profiler (v4.2.1, Molecular Devices) software. Zebrafish Z-projection images were divided into 6 regions – plexus and 5 regions outside (bins). Area of cells was quantified for each region using Cell Profiler and percentage of cells (from total) was calculated per each region and plotted in a graph. Invasion potential was calculated as area under the curve for all cells that extravasated and invaded outside of the vasculature region.

Mass spectrometry–quantitative proteomics

Conditioned medium was produced by WM983B FKBP-FRB ± Rapalog (5 nM) in serum free medium. After 24 h, supernatant was collected, centrifuged at 300 \times g for 10 min and concentrated using a 3 kDa filter. For each of the three conditions, four biological replicates were prepared (cells culture medium, prepared the same way, was used as a control). Following a Pierce™ 660 nm protein assay quantification (ref. n°22660, Thermo Fisher Scientific), 2 μ g of each protein extract were digested using the automated Single Pot Solid Phase enhanced Sample Preparation (SP3) protocol as described in ref. 66 on the Bravo AssayMAP platform (Agilent Technologies). In brief, each protein extract was reduced with 12 mM dithiothreitol (DTT) and alkylated using 40 mM iodoacetamide (IAM) at 37 °C and 25 °C, respectively. A mixture of hydrophilic and hydrophobic magnetic beads was used to clean up the proteins at a ratio of 125:1 beads:proteins (Sera-Mag Speed beads, Thermo Fisher Scientific). After acetonitrile (ACN) was added to a final concentration of 50%, the beads were allowed to bind to the proteins for 18 min. Protein-bead mixtures were washed twice with 80% ethanol and once with 100% ACN. The protein-bead complexes were digested with trypsin:LysC (Promega, Madison) at a 1:20 ratio overnight at 37 °C. Extracted peptides were cleaned-up using automated C18 solid phase extraction with the AssayMAP 5 μ L C18 cartridges (ref. n°5190-6532) on the same platform. After elution with 70% ACN, the resulting peptide mixture was evaporated using a speed-vac (Thermo Fisher Scientific), reconstituted in 2% ACN and 0.1% FA, and analyzed by nanoLC-MS/MS on a nanoUPLC system (nanoAcuityUPLC, Waters) coupled to a quadrupole-Orbitrap mass spectrometer (Q-Exactive HF-X, Thermo Scientific). Peptide separation was performed on an ACQUITY UPLC® Peptide BEH C18 Column (250 mm \times 75 μ m with 1.7 μ m diameter particles) and an ACQUITY UPLC® M-Class Symmetry® C18 Trap Column (20 mm \times 180 μ m with 5 μ m diameter particles; Waters). The solvent system consisted of 0.1% formic acid (FA) in water (solvent A) and 0.1% FA in ACN (solvent B). Samples were loaded into the enrichment column over 3 min at 5 μ L/min with 99% of solvent A and 1% of solvent B. Peptides were eluted at 350 nL/min with the following gradient of solvent B: from 2% to 25% over 53 min, from 25 to 40% over 10 min and from 40 to 90% over 2 min. The system was operated in a data-dependent acquisition mode with automatic switching between MS and MS/MS. Survey full scan MS spectra (mass range 300–1800) were acquired in the Orbitrap at a resolution of 60 K at 200 m/z with an automatic gain control fixed at 3×10^6 and a maximal injection time set to 50 ms. The ten most intense peptide ions in each survey scan with a charge state ≥ 2 were selected for fragmentation. MS/MS spectra were acquired at a resolution of 15 K at 200 m/z , automatic gain control was set to 1×10^5 , and the maximal injection time was set to 50 ms. Peptides were fragmented by higher-energy collisional dissociation with a normalized collision energy set to 27. Peaks selected for fragmentation were automatically included in a dynamic exclusion list for 60 s. To minimize carry-over, a solvent blank injection was performed after each sample. NanoLC-MS/MS data was interpreted to do label-free extracted ion chromatogram-based differential analysis. Searches were done using Mascot software (version 2.5.1, MatrixScience) against a composite database including *Homo sapiens* and *Bos taurus* protein sequences, which were downloaded from UniProtKB-SwissProt (28-07-2021; 26.031 sequences, Taxonomy

ID: 9913 and 9606 respectively) to which common contaminants and decoy sequences were added. Spectra were searched with a mass tolerance of 5 ppm in MS mode and 0.05 Da in MS/MS mode. One trypsin missed cleavage was tolerated and the minimum peptide length was set to 7 amino acids. Carbamidomethylation of cysteine residues was set as a fixed modification. Oxidation of methionine residues and acetylation of proteins n-termini were set as variable modifications. Identification results were imported into the Proline software (version 2.2.0)⁶⁷ and validated. The maximum false discovery rate was set at 1% at peptide and protein levels with the use of a decoy strategy. Peptides abundances were extracted with cross assignment between all samples. Protein abundances were computed using the best ion of the unique peptide abundances normalized at the peptide level using the median. To be considered, proteins must be identified in at least three out of the four replicates in at least one condition. The imputation of the missing values and differential data analysis were performed using the open-source ProStaR software (version 1.30.7)⁶⁸. Imputation of missing values was done using the approximation of the lower limit of quantification by the 2.5% lower quantile of each replicate intensity distribution ("det quantile"). A Limma moderated t-test was applied on the dataset to perform differential analysis. The adaptive Benjamini-Hochberg procedure was applied to adjust the *p* values and False Discovery Rate. The mass spectrometry proteomics data have been deposited to the ProteomeXchange Consortium via the PRIDE partner repository⁶⁹ with the dataset identifier PXD042007.

Transcriptomic analysis

Patient-derived cell lines. WM1862, WM983A, WM983B. RNA integrity was assessed by Bioanalyzer (total RNA Pico Kit, 2100 Instrument, Agilent Technologies, Palo Alto, CA, USA). All samples had RNA integrity numbers above 9.5. Sequencing libraries were prepared using "NEBNext Ultra II Directional RNA Library Prep Kit for Illumina" combined with "NEB Ultra II polyA mRNA magnetic isolation" for mRNA enrichment (New England Biolabs, Ipswich, MA, USA). Libraries were pooled and sequenced (single-end, 100 bp) on a NextSeq2000 according to the manufacturer's instructions (Illumina Inc., San Diego, CA, USA). For each sample, quality control was carried out and assessed with the NGS Core Tool FastQC⁷⁰. Sequence reads (minimum 33 Million per sample) were mapped to *Homo Sapiens* genome version GRCh38 using STAR⁷¹ to obtain a BAM (Binary Alignment Map) file. An abundance matrix was generated based on read counts identified by Featurecounts⁷² using default parameters. At last, differential expression analyses were performed using the DEseq2⁷³ package of the Bioconductor framework for RNASeq data⁷⁴. Up- and down-regulated genes were selected based on their adjusted *p*-value (<0.01). Functional enrichment analyses were performed using STRING v11⁷⁵ and Gene Ontology⁷⁶. Bubble plots and heat maps (Fig. 1A) were generated using GraphPad Prism 9 (version 9.5.1 for Windows). Raw data (FASTQ files) are available at the EMBL-EBI ArrayExpress archive (Accession number E-MTAB-13165).

Statistics & reproducibility

Statistical analysis of the results was done using GraphPad Prism 10 (version 10.4.0 for Windows). Unless stated otherwise, Mann-Whitney test, two-tailed (two groups) or Kruskal-Wallis test with Dunn's multiple comparison post hoc test (3 groups) was performed as specified in the respective figure legends. Quantitative proteomics and transcriptomic analysis have dedicated statistical methodologies specified above. Illustrations of the statistical analyses are displayed in the figures as the mean +/- standard deviation (SD). *P* values smaller than 0.05 were considered as statistically significant. * *p* < 0.05; ** *p* < 0.01; *** *p* < 0.001; **** *p* < 0.0001. No statistical method was used to pre-determine sample size. No data were excluded from the analyses. The experiments were not randomized and not blinded, with the exception

of analysis of patient biopsies presented in Fig. 2 where the quantification was done in a blinded setup. Regions of interest were randomly selected per each patient sample, reaching 240 individual regions, which were randomized and then scored. Investigators were blinded to allocation during experiments and outcome assessment.

Reporting summary

Further information on research design is available in the Nature Portfolio Reporting Summary linked to this article.

Data availability

Proteomics: The mass spectrometry proteomics data have been deposited to the ProteomeXchange Consortium via the PRIDE partner repository⁶⁹ with the dataset identifier **PXD042007**. **Transcriptomics:** Raw data (FASTQ files) are available at the EMBL-EBI ArrayExpress archive with accession number **E-MTAB-13165**. Source data are provided with this paper.

Code availability

All codes written for this article are available on GitHub, to improve reproducibility, the repository was linked to Zenodo⁶⁵, [<https://zenodo.org/records/14924796>].

References

1. Dillekås, H., Rogers, M. S. & Straume, O. Are 90% of deaths from cancer caused by metastases? *Cancer Med.* **8**, 5574–5576 (2019).
2. Braeuer, R. R., Zigler, M., Villares, G. J., Dobroff, A. S. & Bar-Eli, M. Transcriptional control of melanoma metastasis: The importance of the tumor microenvironment. *Semin. Cancer Biol.* **21**, 83–88 (2011).
3. Hua, H., Li, M., Luo, T., Yin, Y. & Jiang, Y. Matrix metalloproteinases in tumorigenesis: an evolving paradigm. *Cell. Mol. Life Sci. CMLS* **68**, 3853–3868 (2011).
4. Zoncu, R. & Perera, R. M. Emerging roles of the MiT/TFE factors in cancer. *Trends Cancer* **9**, 817–827 (2023).
5. Medina, D. L. et al. Transcriptional activation of lysosomal exocytosis promotes cellular clearance. *Dev. Cell* **21**, 421–430 (2011).
6. Ballabio, A. & Bonifacino, J. S. Lysosomes as dynamic regulators of cell and organismal homeostasis. *Nat. Rev. Mol. Cell Biol.* **21**, 101–118 (2020).
7. Naegeli, K. M. et al. Cell invasion in vivo via rapid exocytosis of a transient lysosome-derived membrane domain. *Dev. Cell* **43**, 403–417.e10 (2017).
8. Bian, B. et al. Cathepsin B promotes colorectal tumorigenesis, cell invasion, and metastasis. *Mol. Carcinog.* **55**, 671–687 (2016).
9. Corrotte, M. & Castro-Gomes, T. Chapter One - Lysosomes and plasma membrane repair. in *Current Topics in Membranes* (ed. Andrade, L. O.) vol. 84 1–16 (Academic Press, 2019).
10. Johnson, D. E., Ostrowski, P., Jaumouillé, V. & Grinstein, S. The position of lysosomes within the cell determines their luminal pH. *J. Cell Biol.* **212**, 677–692 (2016).
11. Korolchuk, V. I. et al. Lysosomal positioning coordinates cellular nutrient responses. *Nat. Cell Biol.* **13**, 453–460 (2011).
12. Jia, R. & Bonifacino, J. S. Lysosome Positioning Influences mTORC2 and AKT Signaling. *Mol. Cell* **75**, 26–38.e3 (2019).
13. Mathur, P. et al. Transcription factor EB regulates phosphatidylinositol-3-phosphate levels that control lysosome positioning in the bladder cancer model. *Commun. Biol.* **6**, 1–14 (2023).
14. Steffan, J. J., Snider, J. L., Skalli, O., Welbourne, T. & Cardelli, J. A. Na⁺/H⁺ exchangers and RhoA regulate acidic extracellular pH-induced lysosome trafficking in prostate cancer cells. *Traffic Cph. Den.* **10**, 737–753 (2009).
15. Hämäläistö, S. & Jäättelä, M. Lysosomes in cancer - living on the edge (of the cell). *Curr. Opin. Cell Biol.* **39**, 69–76 (2016).

16. Jerabkova-Roda, K., Marwaha, R., Das, T. & Goetz, J. G. Organelle morphology and positioning orchestrate physiological and disease-associated processes. *Curr. Opin. Cell Biol.* **86**, 102293 (2024).
17. Pu, J., Guardia, C. M., Keren-Kaplan, T. & Bonifacino, J. S. Mechanisms and functions of lysosome positioning. *J. Cell Sci.* **129**, 4329–4339 (2016).
18. Dykes, S. S. et al. The Arf-like GTPase Arl8b is essential for three-dimensional invasive growth of prostate cancer in vitro and xeno-graft formation and growth in vivo. *Oncotarget* **7**, 31037–31052 (2016).
19. Gutierrez-Ruiz, O. L. et al. Ectopic expression of DOCK8 regulates lysosome-mediated pancreatic tumor cell invasion. *Cell Rep.* **42**, 113042 (2023).
20. Kundu, S. T. et al. TMEM106B drives lung cancer metastasis by inducing TFEB-dependent lysosome synthesis and secretion of cathepsins. *Nat. Commun.* **9**, 2731 (2018).
21. Machado, E. et al. Regulated lysosomal exocytosis mediates cancer progression. *Sci. Adv.* **1**, e1500603 (2015).
22. Wu, P.-H. et al. Lysosomal trafficking mediated by Arl8b and BORG promotes invasion of cancer cells that survive radiation. *Commun. Biol.* **3**, 620 (2020).
23. Legrand, M. et al. Protein dynamics at invadopodia control invasion–migration transitions in melanoma cells. *Cell Death Dis.* **14**, 190 (2023).
24. Jacob, A. & Prekeris, R. The regulation of MMP targeting to invadopodia during cancer metastasis. *Front. Cell Dev. Biol.* **3**, 4 (2015).
25. Nair, S. V., Narendraev, N. D., Nambiar, R. P., Kumar, R. & Srinivasula, S. M. Naturally occurring and tumor-associated variants of RNF167 promote lysosomal exocytosis and plasma membrane resealing. *J. Cell Sci.* **133**, jcs239335 (2020).
26. Moamer, A. et al. A role for kinesin-1 subunits KIF5B/KLC1 in regulating epithelial mesenchymal plasticity in breast tumorigenesis. *EBioMedicine* **45**, 92–107 (2019).
27. Wang, Q. et al. LAMP1 expression is associated with poor prognosis in breast cancer. *Oncol. Lett.* **14**, 4729–4735 (2017).
28. Akbani, R. et al. Genomic classification of cutaneous melanoma. *Cell* **161**, 1681–1696 (2015).
29. Kapitein, L. C. et al. Probing intracellular motor protein activity using an inducible cargo trafficking assay. *Biophys. J.* **99**, 2143–2152 (2010).
30. Chen, C.-S., Chen, W.-N. U., Zhou, M., Arttamangkul, S. & Haugland, R. P. Probing the cathepsin D using a BODIPY FL–pepstatin A: Applications in fluorescence polarization and microscopy. *J. Biochem. Biophys. Methods* **42**, 137–151 (2000).
31. Bayle, J. H. et al. Rapamycin analogs with differential binding specificity permit orthogonal control of protein activity. *Chem. Biol.* **13**, 99–107 (2006).
32. Hooikaas, P. J. et al. MAP7 family proteins regulate kinesin-1 recruitment and activation. *J. Cell Biol.* **218**, 1298–1318 (2019).
33. Serra-Marques, A. et al. Concerted action of kinesins KIF5B and KIF13B promotes efficient secretory vesicle transport to microtubule plus ends. *eLife* **9**, e61302 (2020).
34. Mulligan, R. J. et al. Collapse of late endosomal pH elicits a rapid Rab7 response via the V-ATPase and RILP. *J. Cell Sci.* **137**, jcs261765 (2024).
35. Monteiro, P. et al. Endosomal WASH and exocyst complexes control exocytosis of MT1-MMP at invadopodia. *J. Cell Biol.* **203**, 1063–1079 (2013).
36. Vidak, E., Javoršek, U., Vizovišek, M. & Turk, B. Cysteine cathepsins and their extracellular roles: Shaping the microenvironment. *Cells* **8**, 264 (2019).
37. Gocheva, V. et al. Distinct roles for cysteine cathepsin genes in multistage tumorigenesis. *Genes Dev.* **20**, 543–556 (2006).
38. da Costa, A. C. et al. Cathepsin S as a target in gastric cancer. *Mol. Clin. Oncol.* **12**, 99–103 (2020).
39. Chaineau, M., Danglot, L. & Galli, T. Multiple roles of the vesicular-SNARE TI-VAMP in post-Golgi and endosomal trafficking. *FEBS Lett.* **583**, 3817–3826 (2009).
40. Lachuer, H., Le, L., Lévéque-Fort, S., Goud, B. & Schauer, K. Spatial organization of lysosomal exocytosis relies on membrane tension gradients. *Proc. Natl. Acad. Sci.* **120**, e2207425120 (2023).
41. Winkler, J., Abisoye-Ogunniyan, A., Metcalf, K. J. & Werb, Z. Concepts of extracellular matrix remodelling in tumour progression and metastasis. *Nat. Commun.* **11**, 5120 (2020).
42. Kalluri, R. The biology and function of fibroblasts in cancer. *Nat. Rev. Cancer* **16**, 582–598 (2016).
43. Sahai, E. et al. A framework for advancing our understanding of cancer-associated fibroblasts. *Nat. Rev. Cancer* **20**, 174–186 (2020).
44. Hoshino, D. et al. Exosome secretion is enhanced by invadopodia and drives invasive behavior. *Cell Rep.* **5**, <https://doi.org/10.1016/j.celrep.2013.10.050> (2013).
45. Fourriere, L. et al. RAB6 and microtubules restrict protein secretion to focal adhesions. *J. Cell Biol.* **218**, 2215–2231 (2019).
46. Wang, Y. & McNiven, M. A. Invasive matrix degradation at focal adhesions occurs via protease recruitment by a FAK–p130Cas complex. *J. Cell Biol.* **196**, 375–385 (2012).
47. Follain, G. et al. Hemodynamic forces tune the arrest, adhesion, and extravasation of circulating tumor cells. *Dev. Cell* **45**, 33–52.e12 (2018).
48. Schauer, K. et al. Probabilistic density maps to study global endo-membrane organization. *Nat. Methods* **7**, 560–566 (2010).
49. van Bergeijk, P., Hoogenraad, C. C. & Kapitein, L. C. Right time, right place: Probing the functions of organelle positioning. *Trends Cell Biol.* **26**, 121–134 (2016).
50. Marwaha, R. et al. Mechanosensitive dynamics of lysosomes along microtubules regulate leader cell emergence in collective cell migration. 2022.08.03.502740 Preprint at <https://doi.org/10.1101/2022.08.03.502740> (2023).
51. Nakahara, H. et al. Transmembrane/cytoplasmic domain-mediated membrane type 1-matrix metalloprotease docking to invadopodia is required for cell invasion. *Proc. Natl. Acad. Sci.* **94**, 7959–7964 (1997).
52. Wang, L. et al. Spatial topology of organelle is a new breast cancer cell classifier. *iScience* **107229** <https://doi.org/10.1016/j.isci.2023.107229> (2023).
53. Circu, M. L. et al. A novel high content imaging-based screen identifies the anti-helminthic niclosamide as an inhibitor of lysosome anterograde trafficking and prostate cancer cell invasion. *PLOS ONE* **11**, e0146931 (2016).
54. Sero, J. E. et al. Cell shape and the microenvironment regulate nuclear translocation of NF-κB in breast epithelial and tumor cells. *Mol. Syst. Biol.* **11**, 790 (2015).
55. Wu, P.-H. et al. Single-cell morphology encodes metastatic potential. *Sci. Adv.* **6**, eaaw6938 (2020).
56. Heinrich, L. et al. Whole-cell organelle segmentation in volume electron microscopy. *Nature* **599**, 141–146 (2021).
57. Sadok, A. et al. Rho kinase inhibitors block melanoma cell migration and inhibit metastasis. *Cancer Res* **75**, 2272–2284 (2015).
58. Artym, V. V., Yamada, K. M. & Mueller, S. C. ECM degradation assays for analyzing local cell invasion. in *Extracellular Matrix Protocols* 211–219 (Humana Press, 2009) https://doi.org/10.1007/978-1-59745-413-1_15.
59. Duong, T., Goud, B. & Schauer, K. Closed-form density-based framework for automatic detection of cellular morphology changes. *Proc. Natl. Acad. Sci.* **109**, 8382–8387 (2012).
60. Schindelin, J. et al. Fiji: an open-source platform for biological-image analysis. *Nat. Methods* **9**, 676–682 (2012).

61. Goldman, M. J. et al. Visualizing and interpreting cancer genomics data via the Xena platform. *Nat. Biotechnol.* **38**, 675–678 (2020).
62. Stirling, D. R. et al. CellProfiler 4: improvements in speed, utility and usability. *BMC Bioinforma.* **22**, 433 (2021).
63. Lawson, N. D. & Weinstein, B. M. In vivo imaging of embryonic vascular development using transgenic zebrafish. *Dev. Biol.* **248**, 307–318 (2002).
64. Stoletov, K. et al. Visualizing extravasation dynamics of metastatic tumor cells. *J. Cell Sci.* **123**, 2332–2341 (2010).
65. Jerabkova-Roda, K. Peripheral positioning of lysosomes supports melanoma aggressiveness <https://doi.org/10.5281/zenodo.1492479> (2025).
66. Hughes, C. S. et al. Single-pot, solid-phase-enhanced sample preparation for proteomics experiments. *Nat. Protoc.* **14**, 68–85 (2019).
67. Bouyssié, D. et al. Proline: an efficient and user-friendly software suite for large-scale proteomics. *Bioinformatics* **36**, 3148–3155 (2020).
68. Wieczorek, S. et al. DAPAR & ProStaR: software to perform statistical analyses in quantitative discovery proteomics. *Bioinformatics* **33**, 135–136 (2017).
69. Perez-Riverol, Y. et al. The PRIDE database resources in 2022: a hub for mass spectrometry-based proteomics evidences. *Nucleic Acids Res.* **50**, D543–D552 (2022).
70. Wingett, S. W. & Andrews, S. FastQC: A quality control tool for high throughput sequence data. *F1000Res* **7**, 1338 (2018).
71. Dobin, A. et al. STAR: ultrafast universal RNA-seq aligner. *Bioinformatics* **29**, 15–21 (2013).
72. Liao, Y., Smyth, G. K. & Shi, W. featureCounts: An efficient general purpose program for assigning sequence reads to genomic features. *Bioinformatics* **30**, 923–930 (2014).
73. Love, M. I., Huber, W. & Anders, S. Moderated estimation of fold change and dispersion for RNA-seq data with DESeq2. *Genome Biol.* **15**, 550 (2014).
74. Gentleman, R. C. et al. Bioconductor: open software development for computational biology and bioinformatics. *Genome Biol.* **5**, R80 (2004).
75. Szklarczyk, D. et al. STRING v11: protein–protein association networks with increased coverage, supporting functional discovery in genome-wide experimental datasets. *Nucleic Acids Res.* **47**, D607–D613 (2019).
76. The Gene Ontology Consortium. The gene ontology resource: 20 years and still GOing strong. *Nucleic Acids Res.* **47**, D330–D338 (2019).

Acknowledgements

We thank all members of JGG's PR's and KS' teams for discussions on this topic. JGG is the coordinator of the NANOTUMOR Consortium, a program from ITMO Cancer of AVIESAN (Alliance Nationale pour les Sciences de la Vie et de la Santé, National Alliance for Life Sciences & Health) within the framework of the Cancer Plan (France) that has mostly supported this work, including the teams of KS and PR. Work and people in the lab of JGG are also supported by the INCa (Institut National Du Cancer), La Ligue contre le Cancer, ARC (Association pour la Recherche contre le Cancer), FRM (Fondation pour la Recherche Médicale), the National Plan Cancer initiative, the Region Est, INSERM, University of Strasbourg, RAS Foundation, TDLR (Trailers de la Rose), Club Féminin Lampertheim & Rohan Athlétisme Saverne. Proteomics experiments were supported by the French Proteomic Infrastructure (ProFI FR2048, ANR-10-INBS-08-03). KJR is supported by FRM (post-doctoral fellowship SPF202004011876), NANOTUMOR & INCa (PLBIO 23255). HL is supported by ARC and FRM. KJH is supported by the NANOTUMOR consortium and Taiwan National Science and Technology Council (NSTC-

112-2917-I-564-038). The imaging was supported by PIC-STR (CRBS, Strasbourg: P. Kessler), QuEST (IGBMC, Illkirch: E. Grandgirard, E. Guiot), PIQ (Illkirch: R. Vauchelles) INCI (Strasbourg: C. Royer, V. Demais) & PICT-IBISA (Institut Curie, Paris) imaging platforms, members of the national infrastructure France-Biolimaging supported by the French National Research Agency (ANR-10-INBS-04). We would like to thank C. Renaud & C. Brubach (HUS, Strasbourg) for technical assistance during the preparation of patient biopsies, T. Galli (IPNP, Paris) for sharing the VAMP7-pHluorin constructs, A-C. Reymann & R. Benoit (IGBMC, Illkirch) for sharing their resources, F. Saltel & B. Bonnard (BRIC, Bordeaux) for their contribution on invadopodia analysis, D. Sampaio Goncalves (IGBMC, Illkirch) for help with ImageJ macro writing, Mei Li & A. Perrin (IGBMC, Illkirch) for help with mouse intradermal injections, M. Durik (IGBMC, Illkirch) for valuable feedback on the work and F. Colin (CRBS, Strasbourg) for help with graphical representation of the data. Figure 2A, Fig. S3G were designed using silhouettes from Servier Medical Art, licensed under a Creative Commons Attribution 4.0 Unported License (CC:BY 4.0) [<https://creativecommons.org/licenses/by/4.0/deed.en>].

Author contributions

K.J.R., V.H., K.S., P.R. and J.G.G. conceived the project and designed the experiments. K.J.R. performed most of the experiments and analysis. K.J.R., A.M., R.K., H.J., L.M.L., P.C., E.S. and P.R. performed collagen gel invasion assays and invadopodia experiments. K.J.R., N.A. and M.P. performed zebrafish experiments. K.J.R. and I.B. performed CLEM experiments. K.J.H. performed E.M. analysis. L.B., O.L., V.H. and K.J.R. performed mice experiments. C.B.M. was involved in organelle positioning imaging and analysis. V.M. analyzed TCGA data. Q.F. and F.G. designed and performed cytometry analysis. A.L. and O.L. performed molecular biology. K.J.R. performed and analyzed micro-patterning experiments using tools developed by H.L. A.P., T.S., A.M., O.L., V.H. and R.C. performed and analyzed RNAseq experiments. A.H., F.D. and C.C. performed and analyzed mass spectrometry experiments. D.L. and L.S. provided human biopsies. J.G.G., K.J.R., V.H. designed and drew all graphical elements presented in the figures (except for Fig. 2A, Fig. S3G, specified in acknowledgement). V.H., K.S., P.R. and J.G.G. provided funding. V.H. and J.G.G. supervised the study. K.S. and P.R. co-supervised the study. K.J.R., V.H. and J.G.G. wrote the manuscript, with input from K.S. and P.R. All authors proofread the manuscript.

Competing interests

The authors declare no competing interests.

Additional information

Supplementary information The online version contains supplementary material available at <https://doi.org/10.1038/s41467-025-58528-5>.

Correspondence and requests for materials should be addressed to Katerina Jerabkova-Roda, Kristine Schauer, Philippe Rondé, Vincent Hyenne or Jacky G. Goetz.

Peer review information *Nature Communications* thanks Zhan Gao, and the other, anonymous, reviewer(s) for their contribution to the peer review of this work. A peer review file is available.

Reprints and permissions information is available at <http://www.nature.com/reprints>

Publisher's note Springer Nature remains neutral with regard to jurisdictional claims in published maps and institutional affiliations.

Open Access This article is licensed under a Creative Commons Attribution-NonCommercial-NoDerivatives 4.0 International License, which permits any non-commercial use, sharing, distribution and reproduction in any medium or format, as long as you give appropriate credit to the original author(s) and the source, provide a link to the Creative Commons licence, and indicate if you modified the licensed material. You do not have permission under this licence to share adapted material derived from this article or parts of it. The images or other third party material in this article are included in the article's Creative Commons licence, unless indicated otherwise in a credit line to the material. If material is not included in the article's Creative Commons licence and your intended use is not permitted by statutory regulation or exceeds the permitted use, you will need to obtain permission directly from the copyright holder. To view a copy of this licence, visit <http://creativecommons.org/licenses/by-nc-nd/4.0/>.

© The Author(s) 2025

¹Tumor Biomechanics, Strasbourg, France. ²INSERM UMR_S1109, Strasbourg, France. ³Université de Strasbourg, Strasbourg, France. ⁴Fédération de Médecine Translationnelle de Strasbourg (FMTS), Strasbourg, France. ⁵Equipe Labellisée Ligue Contre le Cancer, Strasbourg, France. ⁶Institut Curie, PSL, CNRS, UMR144 Paris, France. ⁷CNRS UMR7021, Faculté de Pharmacie, Illkirch, France. ⁸Institut Gustave Roussy, INSERM UMR1279, Université Paris-Saclay, Villejuif, France. ⁹Plateforme GENOMAX, Institut thématique interdisciplinaire (ITI) de Médecine de Précision de Strasbourg Transplantex NG, Fédération Hospitalo-Universitaire OMICARE, Strasbourg, France. ¹⁰Service d'Immunologie Biologique, Plateau Technique de Biologie, Pôle de Biologie, Nouvel Hôpital Civil, Hôpitaux Universitaires de Strasbourg, 1 Place de l'Hôpital, 67091 Strasbourg, France. ¹¹Faculté de Médecine, Université de Strasbourg et Clinique Dermatologique, Hôpitaux Universitaires de Strasbourg, Strasbourg, France. ¹²Laboratoire de Spectrométrie de Masse Bio-Organique (LSMBO), IPHC, UMR 7178, CNRS, Université de Strasbourg. Infrastructure Nationale de Protéomique ProFI, FR2048 Strasbourg, France. ¹³CNRS, SNC5055 Strasbourg, France. ¹⁴Present address: Epigenetics and Neurobiology Unit, European Molecular Biology Laboratory, 00015 Rome, Italy. ¹⁵Present address: Université de Paris, CNRS, Institut Jacques Monod, 75013 Paris, France. ¹⁶These authors contributed equally: Kristine Schauer, Philippe Rondé, Vincent Hyenne, Jacky G. Goetz.

 e-mail: katerina.jerabkova@inserm.fr; kristine.schauer@gustaveroussy.fr; philippe.ronde@unistra.fr; hyenne@unistra.fr; jacky.goetz@inserm.fr